

Onset of Tropical Cyclone Rapid Intensification: Evaluating the Response to Length Scales of Sea Surface Temperature Anomalies

CHIBUEZE N. OGUEJIOFOR^a, CHARLOTTE E. WAINWRIGHT,^a JOHNA E. RUDZIN,^{b,c} AND DAVID H. RICHTER^a

^a Department of Civil and Environmental Engineering and Earth Sciences, University of Notre Dame, Notre Dame, Indiana

^b Department of Geosciences, Mississippi State University, Mississippi State, Mississippi

^c Northern Gulf Institute, Mississippi State, Mississippi

(Manuscript received 19 July 2022, in final form 10 May 2023, accepted 12 May 2023)

ABSTRACT: Predicting the rapid intensification ($>15.0 \text{ m s}^{-1}$ increase in 10 m wind speed over 24 h or less) of tropical cyclones (TC) remains a challenge in the broader context of numerical weather prediction largely due to their multiscale dynamics. Ocean observations show that the size and magnitude of sea surface temperature (SST) anomalies associated with cold wakes and ocean eddies play important roles in TC dynamics. In this study, a combination of spectral and structure function analyses is utilized to generate realistic realizations of multiscale anomalies characteristic of the SST conditions in which Hurricane Irma (2017) underwent rapid intensification (RI). We investigate the impact of the length scale of these SST anomalies and the role of translation speed on the variance in RI onset timing. Length-scale-induced convective asymmetries, in addition to the mean magnitude of SST anomalies beneath the storm eye, are shown to modulate the variance in RI onset timing. The size of the associated SST length scales relative to the storm size is critical to the magnitude of variance in RI onset timing, as smaller length scales are shown to lack the spatial extent required to induce preferential convective asymmetries. Storm translation speed is also shown to influence the variance in RI onset timing for larger-length-scale ensembles by altering the exposure time of the eye to these SST anomalies. We find that an interplay between SST-induced convective asymmetries, the magnitude of SST anomalies underneath the eye/eyewall, and storm translation speed play crucial roles in modulating the variance in RI onset timing.

SIGNIFICANCE STATEMENT: The characteristics of sea surface temperature (SST) anomalies in the tropical cyclone near-environment are inherently multiscale in nature as a result of interactions between various dynamical processes in the ocean. Assuming a uniform SST beneath storms in numerical simulations limits the predictability of how air-sea interaction affects the physics of rapid intensification (RI). In this study, the influence of realistic multiscale SST anomalies on RI onset timing is investigated. Our results suggest that the length scale of SST anomalies (in addition to its magnitude) modulate the distribution of convection, creating asymmetries around the RMW that can influence the predictability of RI onset. This effect is further modulated by storm translation speed, with the most prominent impact seen in slow-moving storms.

KEYWORDS: Atmosphere; Ocean; Hurricanes/typhoons; Mesoscale processes; Storm environments; Surface temperature

1. Introduction

Sea surface temperature (SST) represents one of the several multiscale environmental parameters modulating hurricane intensity changes, alongside vertical wind shear (VWS), outflow jets, etc. (Holland and Merrill 1984; Emanuel et al. 2004). The magnitude of SST is a principal component of the wind-induced surface heat exchange (WISHE) TC paradigm, which suggests that a positive feedback between surface wind and heat/moisture fluxes is responsible for the intensification of TCs (Emanuel 1986; Holland 1997; Emanuel 1995). Warm SST anomalies as little as 1°C have been shown to significantly increase the intensity of TCs (Emanuel 1988; Schade and Emanuel 1999; Wu et al. 2005) while cold SST anomalies (associated with the wind driven cooling) enhance a negative feedback mechanism which decreases TC intensity.

Warm- and cold-core ocean eddies in the subtropical zonal band of the North Pacific Ocean are examples of SST anomalies. Liu et al. (2012) shows that these mesoscale ocean anomalies have sizes varying from about 30 km to about 170 km and have a life span of up to 50 weeks, covering about 20%–30% of the ocean surface (Chelton et al. 2011; Cheng et al. 2014) and in some cases having a warm anomaly of 1.4°C at the surface and 2.5°C at a depth of 370 m (Yang et al. 2013, 2015). Previous work has shown that the magnitude and sizes of the eddies influence the intensity of TCs as warm-core eddies reduce the storm wind-induced cooling of SST and hence increase TC intensity (Shay et al. 2000; Lin et al. 2005; Wu et al. 2007; Lin et al. 2011; Ma et al. 2017; Rudzin et al. 2019; Anandh et al. 2020; Liu et al. 2021). In one of the more recent attempts to investigate the impacts of a spatial distribution of warm eddies, Sun et al. (2020) examined the influence of the proximity of a fixed-size warm SST anomaly on a stationary storm using a suite of idealized experiments, finding that a warm SST anomaly close to the storm center enhances secondary circulation, increases heat fluxes, and hence strengthens

Corresponding author: Chibueze N. Oguejiofor, coguejio@nd.edu

DOI: 10.1175/JAS-D-22-0158.1

© 2023 American Meteorological Society. This published article is licensed under the terms of the default AMS reuse license. For information regarding reuse of this content and general copyright information, consult the AMS Copyright Policy (www.ametsoc.org/PUBSReuseLicenses).

Brought to you by University of Colorado Libraries | Unauthenticated | Downloaded 08/09/23 05:23 PM UTC

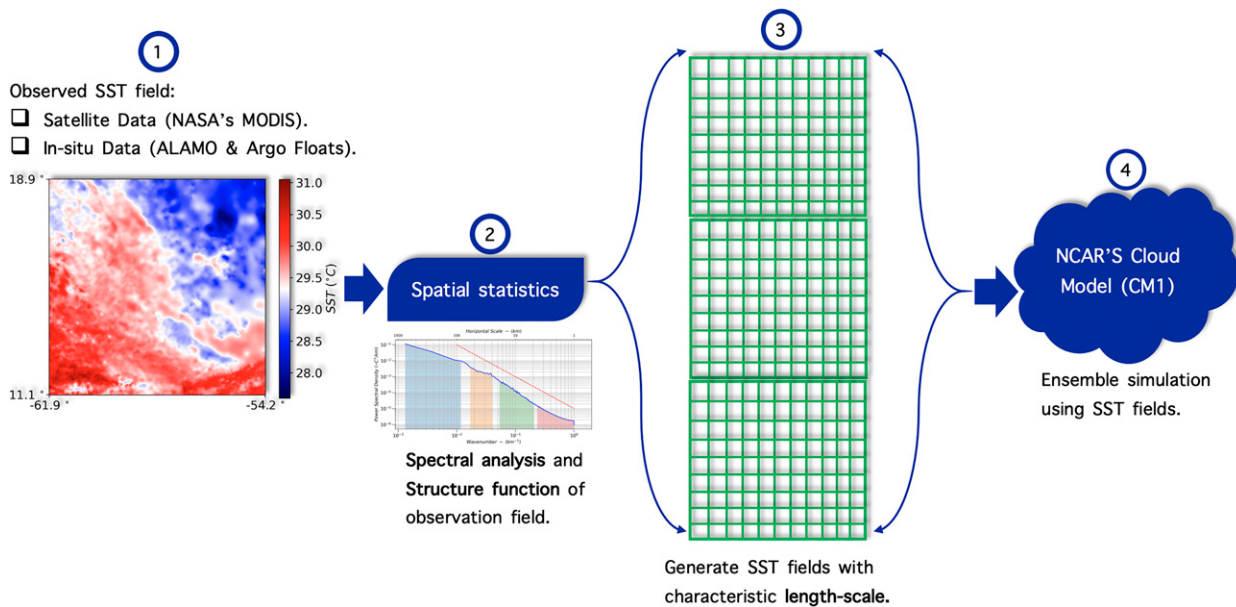


FIG. 1. Broad framework and methodology used in this study.

the storm intensity. An opposite effect was noted for warm SST anomalies positioned farther from the storm center.

In addition to ocean mesoscale eddies, other SST anomalies exist, such as the cold wake generated by a TC, which can vary in size and have a lifespan of up to 4 days (Price et al. 2008; Mrvaljevic et al. 2013), and hence affect the same TC or a subsequent storm. These interactions between TCs and their cold wakes have been investigated extensively in both observational studies (Cione and Uhlhorn 2003; Haakman et al. 2019; Zhang et al. 2019; Sanabia and Jayne 2020) as well as numerical simulations (Chen et al. 2017; Karnauskas et al. 2021). Both types of studies generally agree that the net effect of a cold wake is to reduce the energy supply from warm SSTs, leading to a negative feedback which decreases the TC intensity. This process, however, depends on the translation speed of the TC (Chen et al. 2017).

Despite the advances in understanding the impact of SST on TC intensity changes, there are still open questions. For instance, what is the sensitivity of TC intensity to the multiscale nature of these SST anomalies (i.e., the spatial extent of horizontal heterogeneities in SST anomalies), and how does the size of the TC modulate this sensitivity? Studies have also shown that cold wakes can be advected by preexisting warm eddies (Mrvaljevic et al. 2013), suggesting an interaction of SST anomalies of varying length scales. More generally, how do these multiscale features modulate the timing of the onset of RI?

As described in the literature, the development and persistence of SST anomalies (ocean eddies and cold wakes of TCs), their modulation of air-sea interaction, and how these affect the RI of TCs remain an active area of research. The lack of high-resolution spatiotemporal ocean observations of SST variation in the high-wind TC boundary layer suggests a

gap in present knowledge and a possible oversimplification of physics therein. Furthermore, the dependence of RI on realistic size and spatial distribution of these SST anomalies remain unclear.

In this study, a geostatistical approach is utilized to understand the impact of the length scale of these SST anomalies on storm intensity using random field theory. SST fields obtained from NASA's Multiscale Ultra High Resolution (MUR) satellite imagery (1 km) provide spatial distribution of these anomalies during the rapid intensification phase of Hurricane Irma (2017). Spatial statistics of this SST field are used to generate multiple realizations of unconditional Gaussian random fields with varying length-scale parameters in order to mimic the spatial extent of realistic SST anomalies. The generated SST fields are used as boundary conditions for idealized model runs using Cloud Model 1 (CM1) (Bryan and Fritsch 2002). This process is shown schematically in Fig. 1. We investigate the impact of varying the SST length scale on subsequent TC dynamics and intensification.

Specific objectives of this study include the following:

- 1) Understanding the interaction between modeled storms and the length scales of SST anomalies. Specifically, we are interested in isolating the impact of these length scales and how they influence the variance in onset of rapid intensification.
- 2) Investigating the impact of storm translation speed on its interaction with SST anomalies. We aim to understand the impact of storm exposure time to these length scales of SST heterogeneities and how this modulates the variance in RI onset timing.

The remainder of this paper is organized as follows: Section 2 describes the broad framework of this study, beginning with the

SST data and statistical analyses used to generate the realistic random SST fields. Following this is the model setup and an explanation of the suite of idealized uncoupled simulations conducted to investigate the impact of length scales of SST heterogeneities on RI, including how this sensitivity is affected by storm translation speed. Section 3 presents the results exploring the variances in the onset timing of rapid intensification and its sensitivity to spatial heterogeneities in SST. Section 3 also explores the sensitivity of the TC translation speed to the length scales of these SST anomalies. Finally, results discussed in section 3 are summarized with concluding remarks in section 4.

2. Data and methodology

a. SST data

Global high-resolution ($0.01^\circ \times 0.01^\circ$ grid) data obtained from NASA's MUR project (Chin et al. 2017) provide a gap-free, gridded dataset of daily SST during the life cycle of Hurricane Irma (2017). The dataset is synthesized by combining multiple level-2 satellite SST datasets including NASA Advanced Microwave Scanning Radiometer for EOS (AMSR-E), the JAXA Advanced Microwave Scanning Radiometer 2 (AMSR-2) on *GCOM-W1*, the Moderate Resolution Imaging Spectroradiometers (MODIS) on the NASA *Aqua* and *Terra* platforms, the U.S. Navy microwave WindSat radiometer, the Advanced Very High Resolution Radiometer (AVHRR) on several NOAA satellites, and in situ SST observations from the NOAA iQuam project (Xu and Ignatov 2010, 2014, 2016). This high-resolution SST product has been used previously to analyze the high-wind environment of hurricanes, with validation using 415 collocated airborne expendable bathythermographs (AXBTs) showing about 70% difference in SST within a $\pm 0.5^\circ\text{C}$ bound and 42% within a $\pm 0.25^\circ\text{C}$ bound (Rudzin et al. 2019). Jaimes de la Cruz et al. (2021) extended this validation by adding in situ measurements from two additional hurricanes [Earl (2010) and Isaac (2012)], leading to an overall SST root-mean-square error (RMSE) of 0.8°C from a total of 1085 data points. We note that for the purpose of this study, the RMSE is of minor importance, as the goal of our methodology is to conduct sensitivity experiments for varying SST length scales, not for getting a response to the exact SST field felt by Irma at that time.

Figures 2a and 2b show the track across the Atlantic followed by Hurricane Irma during its life cycle. The spatial distribution of SST over an $8.0^\circ \times 8.0^\circ$ square grid during 5 September 2017 is shown in Fig. 2c. This square grid is selected at the specific time slice during the RI phase of Hurricane Irma (Fig. 2e) to show the multiscale nature of SST anomalies associated with a typical hurricane environment. As seen in Fig. 2c, there are SST anomalies of varying sizes (length scales) seen in this region. The data follow an approximately Gaussian distribution (Fig. 2d) of SST with a mean of 29.4°C , a variance of 0.23°C^2 . In addition to the high-resolution satellite imagery of SST distribution, several AXBTs and Air-Launched Autonomous Micro Observers (ALAMOs) also made profile measurements of upper ocean conditions in the domain of interest during the RI phase of Hurricane Irma, showing a warm upper ocean

condition necessary for RI (Rudzin et al. 2020; Sanabia and Jayne 2020). See appendix A for a description of ALAMO float measurements relative to Hurricane Irma's path.

b. Mathematical framework: Random field theory

Given a two-dimensional (2D) snapshot of a continuous variable such as SST, the value of SST at a point in space ($\mathbf{x}_1, \mathbf{x}_2, \mathbf{x}_3, \dots, \mathbf{x}_n$) can be assumed to be a random variable $T(\mathbf{x})$ with a characteristic mean, variance, and probability density function. A collection of random variables for all points in space for the above 2D field is defined as a random function and the actual set of values of $T(\mathbf{x})$ that makes up this realization of the random function is known as the regionalized variable (Webster and Oliver 2007).

This regionalized variable can be represented as a stationary random process model with a characteristic structural component (i.e., mean, T_μ) and two random components consisting of one spatially correlated variation (ε) and one uncorrelated variation (ε' ; i.e., noise), as shown in the equation below (Hemingway et al. 2020):

$$T(\mathbf{x}) = T_\mu + \varepsilon(\mathbf{x}) + \varepsilon'(\mathbf{x}). \quad (1)$$

The spatially correlated component is relevant in our study of SST variation as it can be interpreted as a measure of the spatial coherence of the SST heterogeneity. This random component can be assumed to be drawn from a distribution with zero mean and a covariance function given by

$$C(\mathbf{h}) = E[\varepsilon(\mathbf{x})\varepsilon(\mathbf{x} + \mathbf{h})], \quad (2)$$

where \mathbf{x} is a measure of the distance metric of separation between the value of \mathbf{x} at one location and \mathbf{x} at another location (hereafter referred to as lag distance). For small lag distances (\mathbf{h}), under the assumption of second-order stationarity, the expected difference between the value of the random variable at one point (\mathbf{x}) and ($\mathbf{x} + \mathbf{h}$) would be zero (Matheron 1965); thus,

$$E[T(\mathbf{x}) - T(\mathbf{x} + \mathbf{h})] = 0. \quad (3)$$

Hence, the variance is given by

$$\begin{aligned} \text{var}[T(\mathbf{x}) - T(\mathbf{x} + \mathbf{h})] &= E[\{(T(\mathbf{x}) - T(\mathbf{x} + \mathbf{h}))^2\}], \\ &= 2\gamma(\mathbf{h}), \end{aligned} \quad (4)$$

where $\gamma(\mathbf{h})$ is called the semivariance at lag \mathbf{h} (Cressie 1993).

The structure function of a 2D SST field is computed using the semivariance $\gamma(\mathbf{h})$ for every possible pair of data points separated by the particular lag vector \mathbf{h} , $m(\mathbf{h})$:

$$\begin{aligned} \gamma(\mathbf{h}) &= \frac{1}{2} E[\{(T(\mathbf{x}) - T(\mathbf{x} + \mathbf{h}))^2\}] \\ &= \frac{1}{2m(\mathbf{h})} \sum_{i=1}^{m(\mathbf{h})} (T(\mathbf{x}) - T(\mathbf{x} + \mathbf{h}))^2. \end{aligned} \quad (5)$$

A plot of the structure function (variogram) computed from the observed data is called the experimental variogram, which can be fitted with known statistical models possessing particular properties (positive definiteness, continuity, differentiability, etc.)

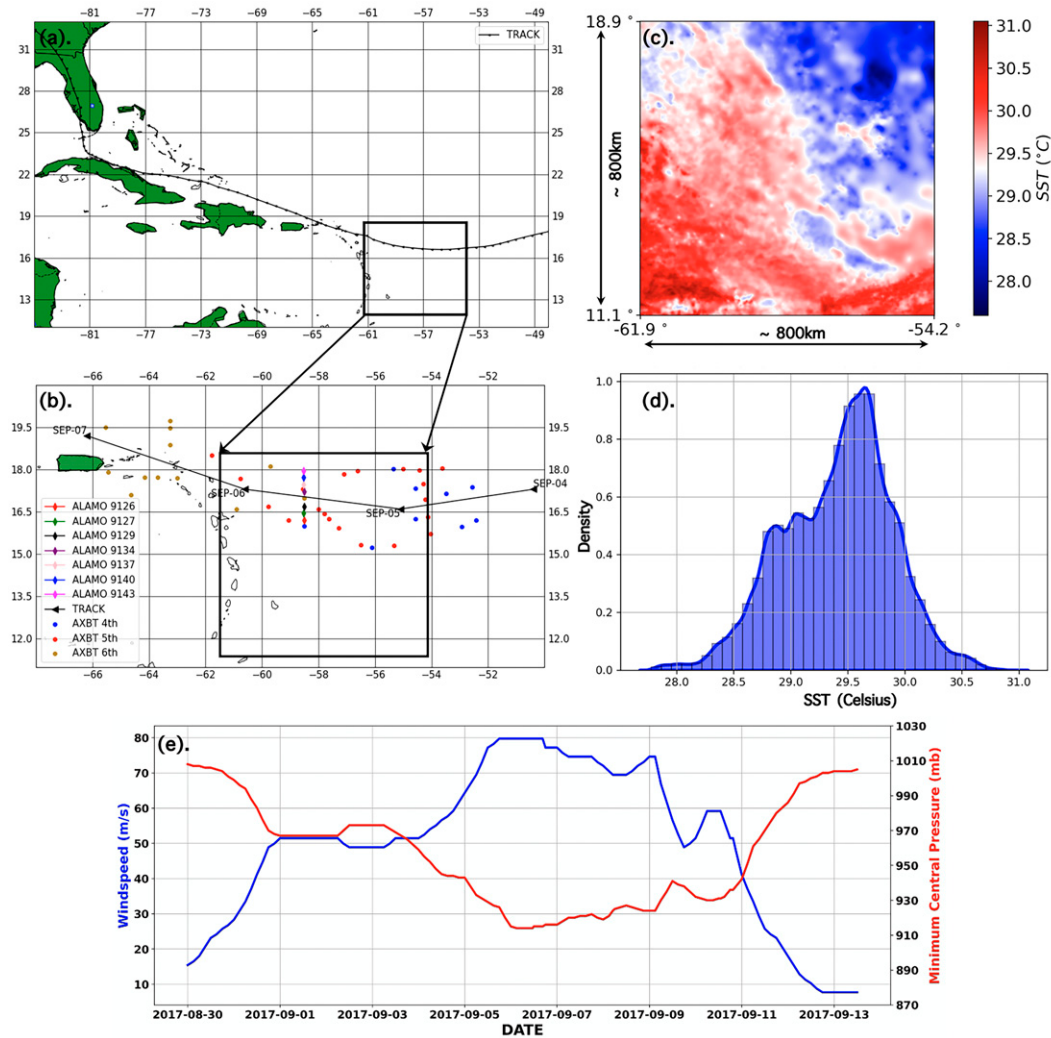


FIG. 2. (a) Map showing the track traversed by Hurricane Irma (2017). (b) Map showing the distribution of ocean instruments measuring ocean conditions of Hurricane Irma (ALAMO floats and AXBTs) along the track of Hurricane Irma. (c) NASA's MODIS 1 km satellite product showing the sea surface temperature conditions of the boxed field in (a) and (b) on 5 Sep 2017. (d) Probability density distribution of SST field shown in (c). (e) A plot of the International Best Track Archive for Climate Stewardship (IBTrACS) intensity chart for Hurricane Irma.

from which information about the field is extracted (Journel and Huijbregts 1978; Clark 1979).

The structure function has a general shape of increasing in value with lag distance until it plateaus at a value of semivariance known as the *sill* for a given lag distance (*range*). The range is the lag distance at which the semivariance is maximized (i.e., the lag distance at which point samples are completely uncorrelated); hence, it is a measure of the length scale of spatial continuity seen in the 2D distribution of SST values. The structure function can be used to generate multiple realizations (simulations) of spatially correlated 2D SST fields.

c. Structure function and spectral analysis of SST field

The SST field is downscaled to a 2 km resolution product (Fig. 2c) from which the first- and second-order moments

(mean and variance) are extracted. The structure function (experimental variogram) is then calculated from the domain shown in Fig. 2c using Eq. (5). The variogram is computed numerically over the domain using a bin size of 45 and a maximum lag of 560 km. SST follows a general trend of decrease in magnitude from the equator to the poles due to uneven solar radiation. However, following a similar rationale by Doney et al. (2003), the size of the domain was chosen after manual investigation to minimize the inherent spatial heterogeneity associated with a latitude dependence of SST while preserving the spatial extent necessary for capturing the multiscale nature of SST anomalies (5–200 km). This choice also provides a justification for computing an omnidirectional variogram which assumes an isotropic field (i.e., spatial continuity has no preferred direction/orientation). For larger

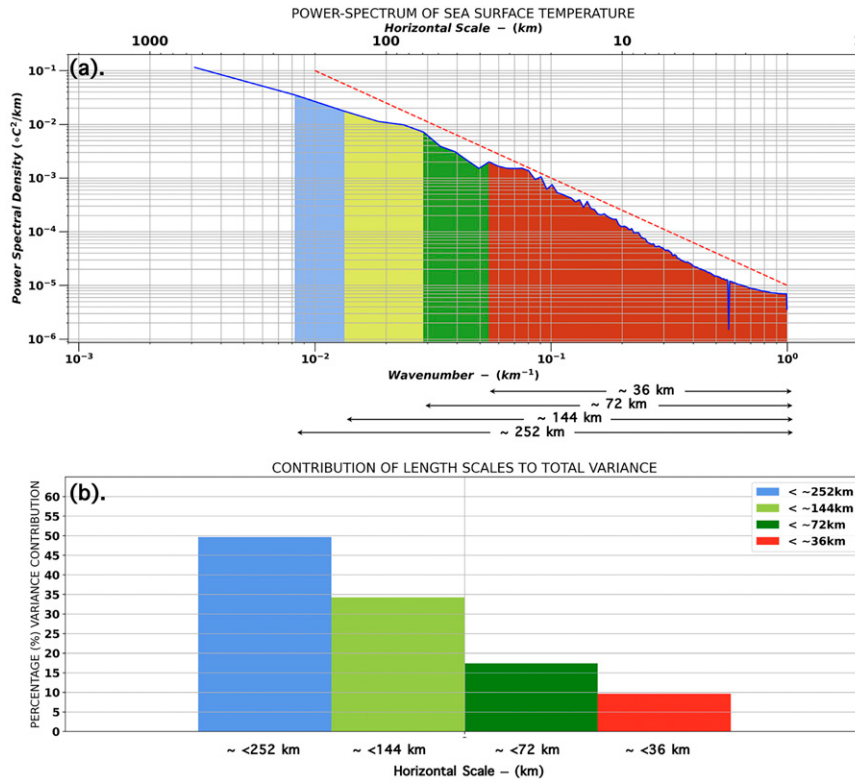


FIG. 3. (a) 2D power spectral density curve of the SST field shown in Fig. 2c, with the red line showing the $7/5$ slope line. (b) Percentage variance contribution from different length scales; the full integral of (a) represents the total variance.

domain sizes with inherent anisotropy, spatial continuity in preferred directions are often captured using directional variograms for the major axes (N–S and E–W). Furthermore, this study is focused more on the influence of the length scales of SST anomalies on the onset of RI, and not anisotropic effects. More information on the experimental variogram and anisotropic effects in the domain is detailed in appendix B.

The experimental variogram computed was then fitted with a common function known as the spherical model:

$$\gamma(h) = \begin{cases} c \left[\frac{3h}{2a} - \frac{1}{2} \left(\frac{h}{a} \right)^3 \right], & \text{for } h \leq a, \\ c, & \text{for } h > a, \end{cases} \quad (6)$$

where a is the range and c is the sill. The spherical model is chosen for use in this study because it is simple, ubiquitous in use in geostatistics, and known for ease of interpretation (Clark 1979), not necessarily for any specific physical reason. For an ideal case, this represents a function with a small value of semivariance at the origin representative of distances smaller than the sampling interval (2 km) or unresolved submesoscale (defined here as <2 km) variance c_0 . This function then increases in value with increasing lag distance until it plateaus out for a lag distance h (the range), roughly representative of the maximum diameter of spatial continuity. The range represents the maximum length scale of continuity,

corresponding in this study to SST anomalies of interest, e.g., ocean mesoscale eddies and cold wakes. The value of the semivariance c at the range represents the maximum variance in the 2D field. The experimental variogram was fitted using a theoretical spherical variogram with $c_0 = 0.0^\circ\text{C}^2$, $c = 0.23^\circ\text{C}^2$ (variance of the 2D SST field), and a variable range corresponding to the chosen length scale of SST anomalies we wish to simulate.

A power spectral density (PSD) of the SST field (Fig. 3a) is computed from the 2D discrete Fourier transform of the SST fields. The amplitude of the Fourier spectrum is then computed for the norm of wavenumbers (k -spatial frequency) which have been appropriately binned. A plot of the square of the Fourier amplitude against wavenumbers gives the power spectral density and is indicative of the variance distribution at different wavenumbers (length scales)—this is shown in Fig. 3a. Figure 3a shows the PSD of the SST field, with the shaded area under the PSD curve indicative of the variance contribution by specific wavenumber ranges (horizontal scales; note that overlap of the colors at high wavenumbers is implied). The PSD curve is scaled by the area under the curve to extract the appropriate variance used in simulating the random SST fields shown in Fig. 4. Thus, spectral scaling allows the transfer of the appropriate variance contribution from the observed SST field to the simulated SST fields with different length scales.

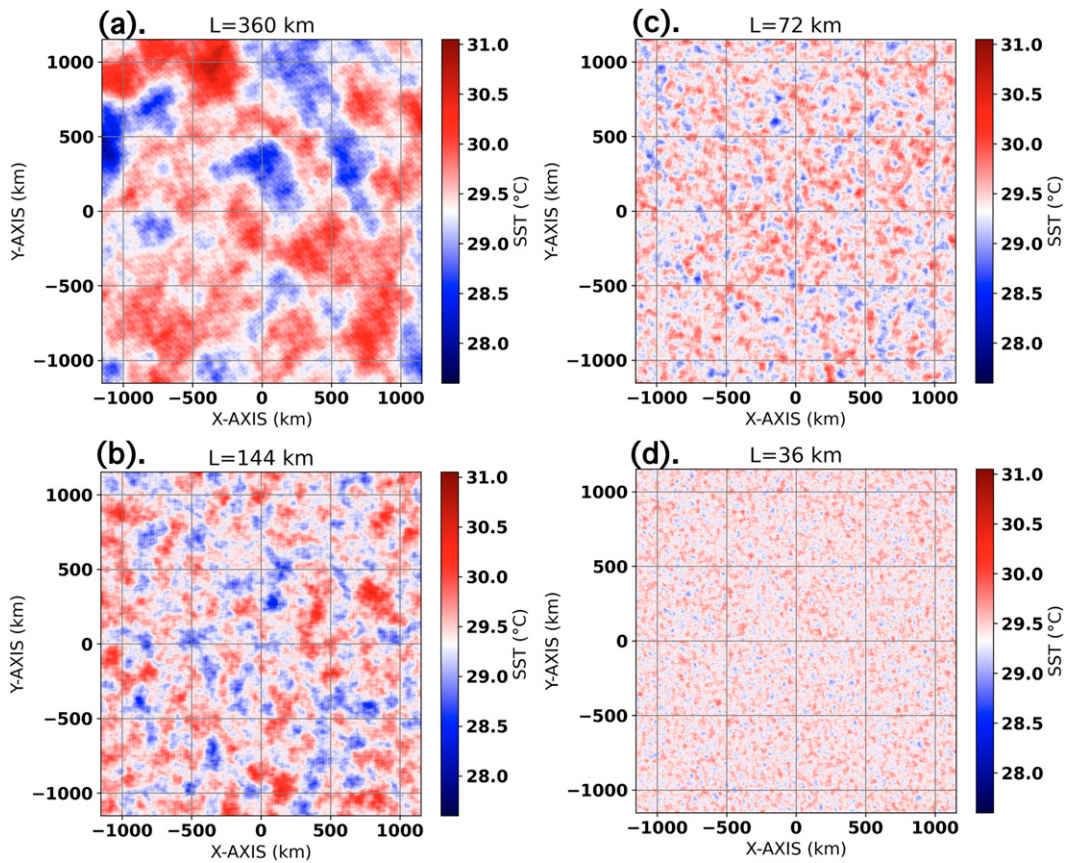


FIG. 4. Sample of SST fields with length scales corresponding to (a) 360, (b) 144, (c) 72, and (d) 36 km.

Figure 3b shows the percentage contribution of different horizontal scales to the total variances seen in the SST field characteristic of when Irma underwent RI. We see clearly that most of the variance is contributed by large-scale SST anomalies (about 50% variance contribution from length scales of ≤ 252 km), while the least variance contribution is attributed to smaller scales (about 10.0% variance contribution from length scales of ≤ 36 km). This justifies our choice of scaling the variance in the simulated fields of different spatial scales generated (in section 2d), despite the mean being kept constant. For completeness, we also later investigate the effect of using the same variance in generating the simulated fields (changing only the spatial scales).

d. Simulated sea surface temperature fields

We investigate the sensitivity of the RI onset timing to SST length scales by generating an ensemble of random fields with the same first- and second-order statistics (mean and variance) as the domain traversed by Hurricane Irma, as well as varying the length scale of spatial continuity (range) of the structure function used to generate the fields. With this, we are able to analyze multiple realizations of stationary, isotropic, Gaussian random fields generated with similar correlation structures as the parent field, only differing by the diameter of

spatial coherence, indicative of characteristic sizes of SST anomalies. Sample synthetic fields are shown in Fig. 4.

Each realization of the random field generated represents one possible SST spatial distribution. As stated above, the assumptions of isotropy (that the SST fields do not have any preferred direction of spatial continuity), weak stationarity (that the mean and variance of the SST fields do not vary with absolute location on the field but with lag distance alone), ergodicity (that the statistical moments of a single realization of the random field in space approach those of the ensemble as the regional boundaries tend to infinity; Webster and Oliver 2007), and Gaussianity (that the random fields generated follows a normal distribution with known mean and variance) are made. The assumption of isotropy is justified for the small domain of interest as there is no observable latitude dependence of SST as would be expected for a larger domain. The assumption of Gaussianity is also justified as the distribution of SST in the parent domain is seen to follow a roughly normal distribution (Fig. 2d).

In addition to these assumptions, the spatial correlation of the fields are approximated using a spherical model as described in section 2b and Eq. (6) above. Recall that the range parameter (h) controls the diameter of spatial continuity in this model; thus, we vary this parameter in generating the random SST fields to simulate specific sizes of SST anomalies

TABLE 1. Summary of the three groups of numerical experiments in this study.

Experiment	Model setup	Description
Length-scale experiment–A		
Sensitivity of RI onset to length scales of SST anomalies (realistic scaling of SST variance)	Initial RMW = 36 km, initial Vmax = 10 m s ⁻¹ , Δx = Δy = 2 km (unstretched)	36 ensemble simulations using time-invariant SST fields with different length scales (36, 72, 144, and 360 km)
Length-scale experiment–B		
Sensitivity of RI onset to length scales of SST anomalies (constant SST variance across length scales)	Initial RMW = 36 km, initial Vmax = 10 m s ⁻¹ , Δx = Δy = 2 km (unstretched)	27 new ensemble simulations using time-invariant SST fields with different length scales (36, 72, and 144 km)
Translation speed experiment		
Sensitivity of translating storms to length scales of SST anomalies	Initial RMW = 36 km, initial Vmax = 10 m s ⁻¹ , Δx = Δy = 2 km (unstretched)	18 ensemble simulations using time varying SST fields (with a length scale of 360 km) with the storm translating from left to right at 2.5 m s ⁻¹ (9 simulations) and 5.0 m s ⁻¹ (9 simulations)

observed in a typical hurricane environment. An ensemble of nine random fields are generated for each of four selected length scales (360, 144, 72, and 36 km) corresponding to multiples of the initial RMW used in the subsequent simulated storms. Figure 4 shows a sample of one random field for each of the specified length scales, clearly illustrating a decrease in the length scale of SST anomalies and associated variance. Notice that the smallest length-scale (36 km) SST field approaches a uniform field as the variations become almost indistinguishable at the scale of the figure.

e. Model setup

The model used in this study is the CM1 model version 20.2.0 (Bryan and Fritsch 2002), which is a three-dimensional, nonhydrostatic solver. Thirty-six sensitivity experiments (9 for each SST length scale) are performed using the SST fields generated above as lower surface boundary conditions. The model intrinsic variability was obtained by initializing the simulation with random potential temperature perturbations of ±0.1 K throughout the entire domain, also for an ensemble size of 9. The simulations are initialized using a modified Rankine vortex for a small sized storm [following the definition of TC size in Carrasco et al. (2014)] with an initial RMW of 36 km and maximum tangential velocity (Vmax) of 10 m s⁻¹. To further isolate the impact of length scales, the same set of experiments above are repeated but the variance for all SST fields (across different length scales) is kept constant, totaling 63 experiments. We note that using the same variance for SST fields having length scales ranging between 360 and 36 km is physically unrealistic, as such sharp SST gradients between small perturbations are rarely observed in reality. Instead, this set of experiments is meant to untangle the interaction between SST variance magnitude and length scale, thereby strengthening our conclusions. In addition to these, a final set of experiments was carried out with a translating storm across the prescribed SST field. Table 1 below summarizes the experiment setup for each group of simulations.

Each experiment is run on a 1152 × 1152 horizontal grid with uniform horizontal grid spacing of 2 km. The vertical grid has 59 levels and is stretched below 5500 m, with 50 m grid spacing near the surface to ensure the boundary layer is appropriately resolved. Above 5500 m, a constant vertical grid spacing of 500 m is used to the domain top at 25 km. The total size of the domain in the horizontal direction is approximately 2300 km × 2300 km. The simulations are set up on an f plane with Coriolis parameter of 5×10^{-5} s⁻¹, using the Morrison double-moment microphysics scheme (Morrison et al. 2005, 2009), and the simple Louis-type planetary boundary layer (PBL) parameterization scheme (Bryan and Rotunno 2009) as a result of their simplicity and wide usage in TC modeling studies. All simulations were run with radiation turned off in order to isolate other complexities of TC dynamics, seeing that this study is focused on the impact of ocean conditions (specifically SST) and its effect on RI onset timing.

The simulations are broken into three specific numerical experiments as detailed below.

1) LENGTH-SCALE EXPERIMENT–A

The simulated TC is initialized using a modified Rankine vortex with an RMW of 36 km, and a maximum wind speed of 10 m s⁻¹ decaying at a radial decay rate of 0.5 until 500 km (radius of zero wind). The vortex was initialized at the center of the domain, with no large-scale pressure gradient acceleration applied to the *u* and *v* components of velocity. Similarly, the vertical wind shear is zero for all simulations which allows a more conducive environment for rapid vortex spin up. The SST fields used in these experiments are the ensemble realizations noted above with varying length scales as shown in Fig. 4. The SST fields are time invariant for this set of experiments.

2) LENGTH-SCALE EXPERIMENT–B

The model setup for this set of experiments remains the same as the length-scale experiment–A with a simple change in variance of the SST fields among the length-scale ensemble.

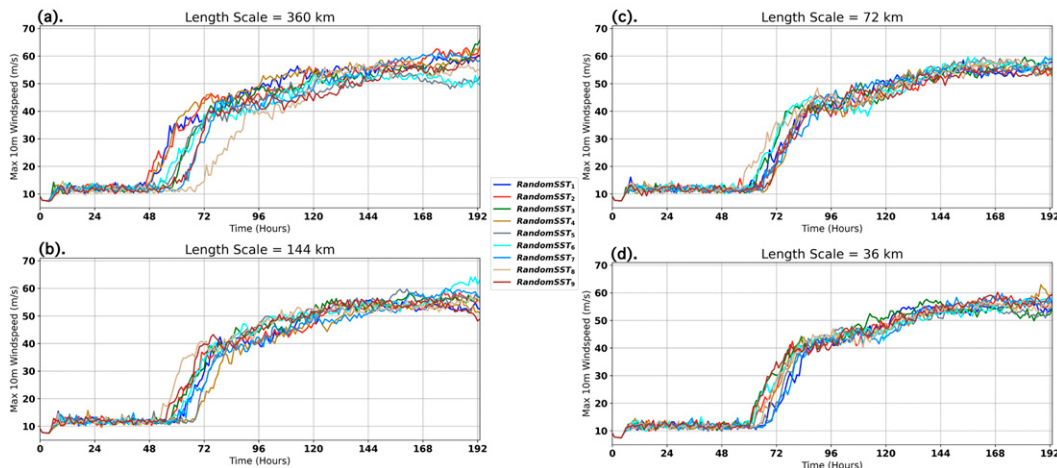


FIG. 5. Intensity plots of modeled storms with initial RMW of 36 km using ensemble SST random fields with length scales of (a) 360, (b) 144, (c) 72, and (d) 36 km.

Instead of the observationally scaled variances (as in length-scale experiment–A), this set of experiments uses a fixed variance (corresponding to the variance of the 360 km length-scale ensemble) for all SST fields generated. Thus, SST fields with length scales of 36, 72, and 144 km would have the same spatial variance as those of 360 km length scale. We note that this effectively implies an unrealistic sharp gradient between SST anomalies in the generated field (specifically in the smaller length scales). However, in combination with length-scale experiment–A, this would further elucidate the dynamical response of RI onset timing to SST length scales apart from their magnitude.

3) TRANSLATING STORM EXPERIMENT

For this set of experiments, unlike the stationary storm experiments above, the effects of storm translation are included to understand the influence of storm exposure to SST anomalies. This experiment uses two translation speeds of 2.5 and 5.0 m s⁻¹ (typical average translation speed for category 4–5 storms; Mei et al. 2012; Kossin 2018), to capture the effect of both realistic storm translation speed and slower-than-average storm translation speed. To minimize the influence of windshear and/or storm related environmental flow on eyewall symmetry, the translation was implemented by updating the lower boundary (SST fields) of the domain at every model time step (Fig. 14). These experiments (using a storm initialized in the way as in experiments A and B above) translate from left to right across SST fields with a length scale of 360 km (10 times the initial RMW).

3. Results and discussion

a. Evaluating the response of stationary storms to SST length scales

1) SENSITIVITY OF MODELED STORMS TO SST LENGTH SCALES

Figures 5a–d show plots of the intensity (in terms of Vmax) of all ensemble members for SST length scales of 360, 144, 72,

and 36 km, respectively, exhibiting differences in the spread of the onset timing of RI. From these plots, there is a clear influence of the length scales on the variance of RI onset time. It is worth noting that there is also a significant spread in the steady-state intensity (particularly after 180 h) among the ensembles for each length scale. However, in this study, we are primarily concerned with the variance in RI onset timing (between 40 and 90 h); hence, most of our analyses are focused on this time span. Storms initialized over SST fields with a length scale of 360 km are seen to have a wider spread in RI onset compared to storms initialized over a 36 km length scale, suggesting a scale dependence of variance in RI onset.

Figure 6a shows a plot of the maximum 10 m wind speed variance ($\sigma_{V_{\text{max}}}^2$) among the ensemble simulations over time, with the black dashed line representing the model intrinsic variability and the solid lines representing different length scales. This figure shows that for all length scales (except 36 and 72 km), the variances in the onset timing of RI is significantly higher than the intrinsic variability of the model. The maximum variance is seen between 40 and 90 h, which corresponds to the range of timing of RI among the ensemble members. The maximum variance during this period is associated with the largest length scale (360 km), and is seen to decrease for smaller length scales. Furthermore, the onset of the increase in variance appears earlier for larger length scales (360 and 144 km). For smaller length scales, however, there is a delay in the timing of the increase in variance of maximum 10 m wind speed (by up to 10 to 20 h—compared to the 360 and 144 km length scale), suggesting a scale-dependent response of modeled storms to RI onset timing despite the domain-mean SST staying roughly the same.

Figure 6b presents the variances in maximum 10 m wind speed against SST anomaly length scale at specified times within the observed range of rapid intensification (50, 60, 70, and 80 h) across the ensemble. From these, there is a noticeable steady increase in the variance of Vmax with length scale. This maximum in Vmax variance is consistent for all

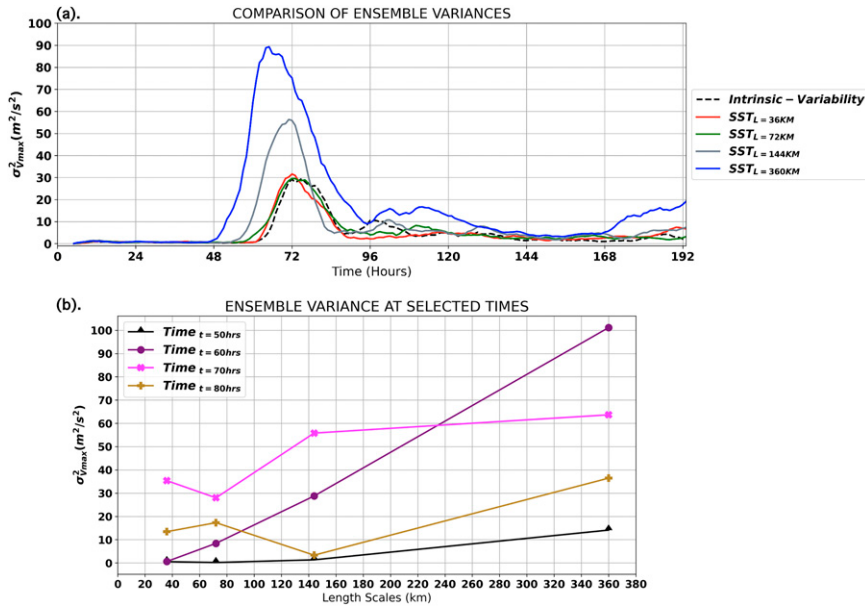


FIG. 6. (a) Variance of maximum 10 m wind speed against integration time for selected length-scale simulations (solid lines) and intrinsic variability of model (dashed black line). (b) Variance of maximum 10 m wind speed for different length scales during selected times corresponding to intensification (50 h: black line; 60 h: purple line; 70 h: magenta line) and postintensification (80 h: golden line), showing a variance peak for a length scale of 360 km.

sampled times (360 km), decreasing for length scales. Minimum variance is seen for length scales smaller than 2 times the initial RMW of the storm. Figures 6a and 6b suggest an interesting dynamical response of the storm to SST anomalies having a length scale at least 2 times that of the initial storm size. To investigate this further, the SST fields corresponding to the ensemble members with the earliest and latest onset of RI (Random SST₁ and Random SST₈) are closely examined in Fig. 7. Figures 7a–d show the SST fields associated with these end members overlaid by the initial RMW. These SST fields represent the lower boundary conditions experienced by the storms simulated in Fig. 5a above (shown by the blue and light-gold solid lines, respectively). From this, it is seen that the magnitude and size of SST anomalies underneath the eye/eyewall plays a crucial role in modulating the timing of RI onset, as might be expected, with warmer SST anomalies within the RMW (Figs. 7a,b, blue line in Fig. 5a) leading to the storm intensifying about 20 h earlier than cold SST anomalies (Figs. 7c,d, light-gold line plot in Fig. 5a).

A visual comparison of convective structures of all simulated storms at day 3 is shown in Fig. 8, indicating the simulated reflectivity at 1 km height (zoomed to a 200 km × 200 km square domain) for all nine ensemble members with an SST length scales of 36, 72, 144, and 360 km. From the last column, there are clear differences in the convective structure and eyewall formation for simulations using different SST fields with the same length scale of spatial continuity. Members 1 and 8 of the last column in Fig. 8 show the reflectivity signatures for the storms initialized over the relatively warm and cool SST anomaly referred to in Fig. 7, clearly illustrating the distinct eye

formation for the former and the scattered/unorganized convection in the latter. It is clear that the magnitude and size of the SST anomaly underneath the eye/eyewall of the storm significantly influences the convective structure and eyewall formation, which consequently affects the timing of the onset of RI. Furthermore, the variance in the mesoscale and convective structures of the storms is seen to increase progressively as the length scales increase up until the maximum at 360 km (last column). The convective structures in the last column (360 km length scale) display, qualitatively speaking, a significant variance among ensemble members as seen in Fig. 8, with member 8 showing unorganized convection with a poorly organized eyewall, uncharacteristic of strong storms. Ensemble members 1, 2, and 4 show well-organized, closed convective structures around the eye, indicative of an intensifying or already-strong storm. An opposite structural variance is seen in the first column (36 km length scale), with all ensemble members (except for 3 and 6) showing an equally weakly organized convective structures. The physical processes underlying the variance in convective structures seen across ensemble members at varying length scales is explored in the following subsections.

To better quantify the preferential convective asymmetries induced by the SST anomalies about the storm RMW, plots of the Pearson's correlation coefficient between both SST and reflectivity as well as SST and surface accumulated rainfall are shown in Fig. 9. This was computed from the values of relevant variables (SST, reflectivity, and surface accumulated rainfall) at each grid point spanning a ≈200 km × 200 km square domain around the domain center, where the storm was initialized (shown in Figs. 7b,d). Figures 9a–d show time

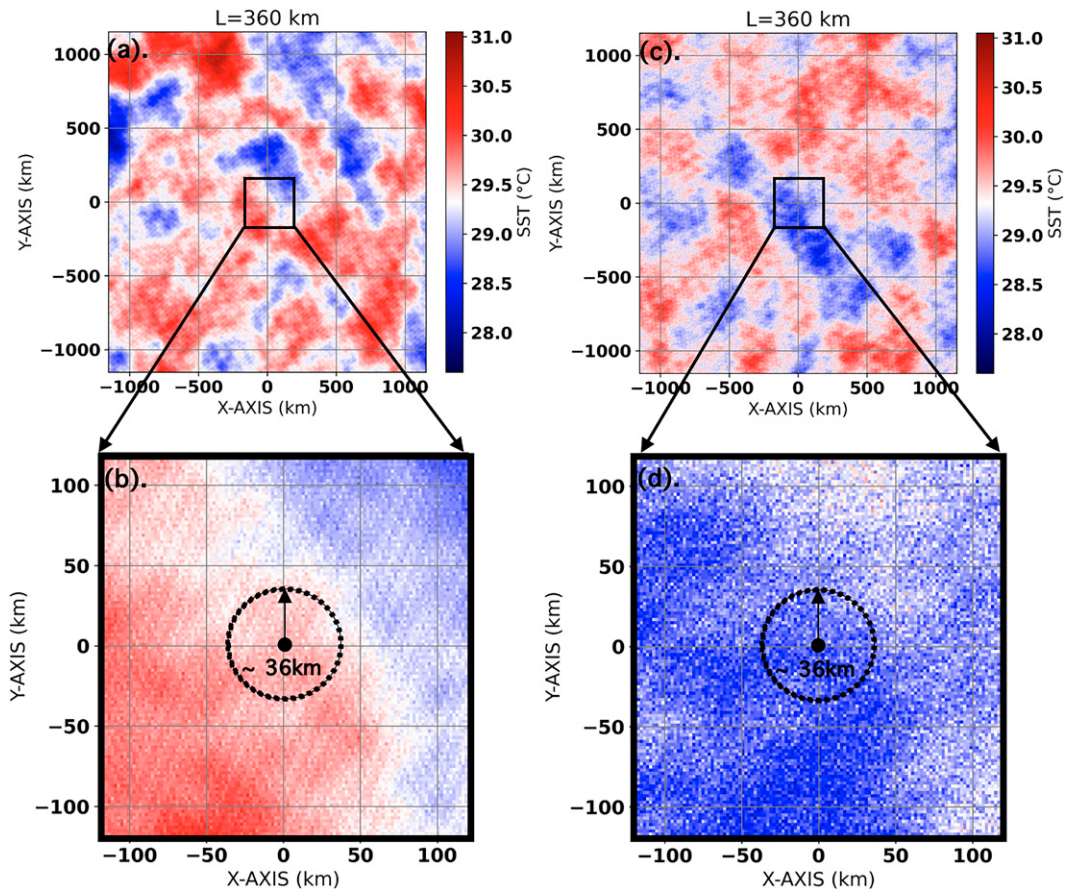


FIG. 7. SST distribution for the ensemble members with (a) delayed RI and (c) early RI. (b),(d) A closer view of the SST near the domain center with the initial RMW of 36 km overlaid, corresponding to Random SST₁ and Random SST₈, respectively, in Fig. 5a.

series between 20 h (well after model spinup) and 100 h (after RI), capturing the evolution of the relationships between SST and reflectivity as well as SST and total surface accumulated rainfall (where the vertical dashed line indicates the onset of RI and the horizontal dashed line indicates the zero correlation line). There is a distinct relationship between convective development and the distribution of SST, depicted by the nonzero correlation coefficients. The case with the fastest RI onset, SST₁, shows a strong positive correlation as RI occurs and continues, with the same pattern seen in the correlation between SST and the surface rainfall. The case with the most delayed RI onset, SST₈, shows a generally weaker, but negative correlation, particularly in the hours leading up to RI.

2) ISOLATING THE CONTRIBUTION OF SST LENGTH SCALES

As introduced in model setup, the core strategy behind our approach is to explore realistic SST anomalies on storm RI, using a spatial stochastic process whose properties are a function of an observed parent field (in our case Hurricane Irma). According to observations, the variance of the SST anomalies

is directly linked to their spatial size, as one might expect (Fig. 3). This raises the question, however, if the modification in RI onset timing seen in the previous section is due solely to the spatial extent and juxtaposition of the SST patches with the initial storm core (i.e., their size), or whether it is the magnitude of the SST anomalies that is the main contributor to the trends seen in RI timing (Fig. 6). Length-scale experiment-B is designed to answer this question. Unlike length-scale experiment-A described above, the ensembles for all length scales have the same SST variance, corresponding to the variance used in the 360 km field (0.114°C^2). With this analyses, we can isolate the impact of the spatial extent of SST anomalies versus their magnitude on the variance in RI onset timing.

Figure 10 presents a plot of the variance of maximum 10 m wind speed (for length-scale experiment-B) among the ensembles. Comparing Fig. 10 to Fig. 6a, we note that the impact of a constant variance in the ensemble SST field realization is primarily to increase the magnitude of the variance seen in RI onset timing for length scales of 144 and 72 km. This is somewhat unsurprising as we expect that using the exact same variance of the 360 km ensemble on the 144 and 72 km fields

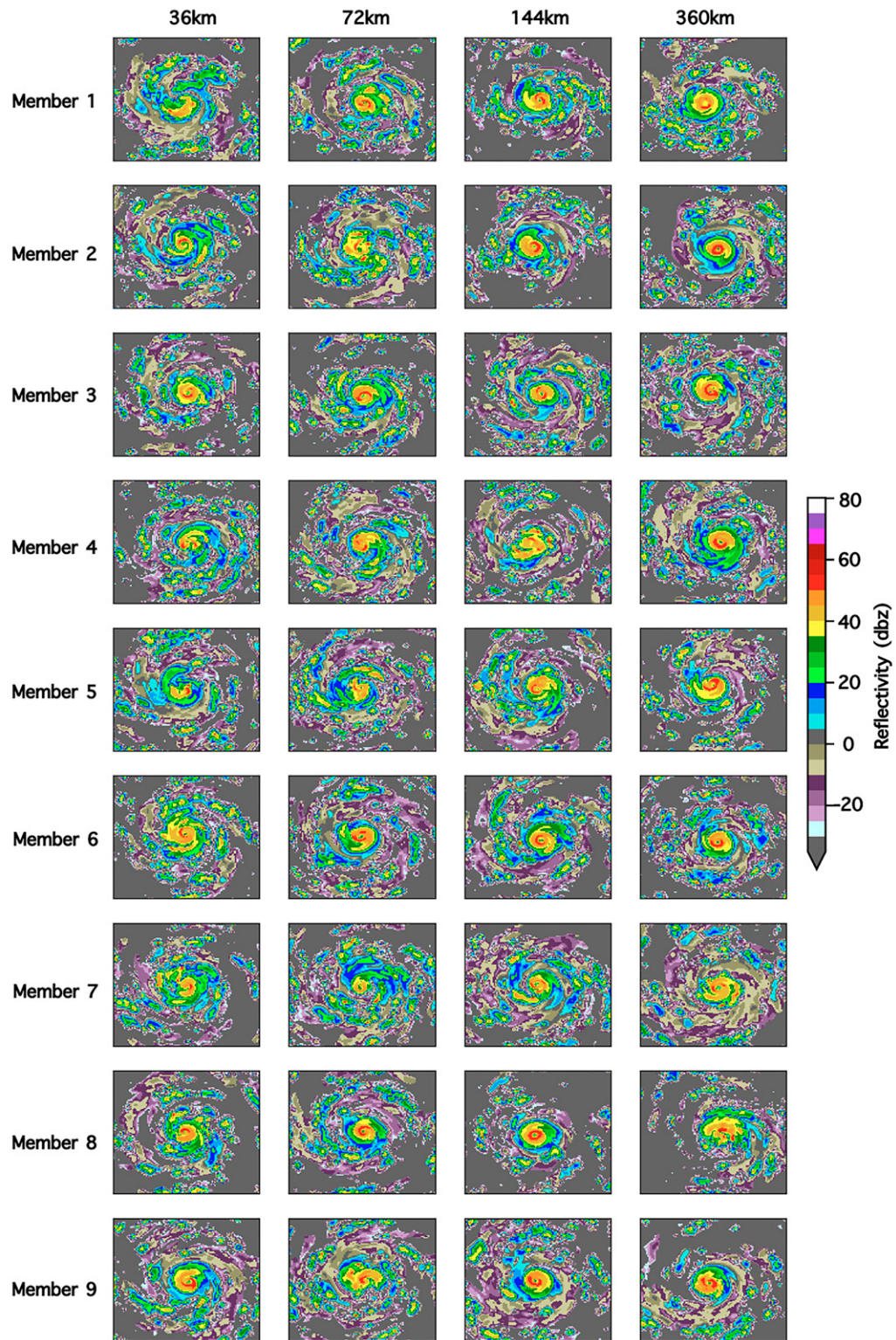


FIG. 8. Ensemble plots of reflectivity (at 1 km height) on model day 3 for length scales of (left to right) 36, 72, 144, and 360 km, respectively.

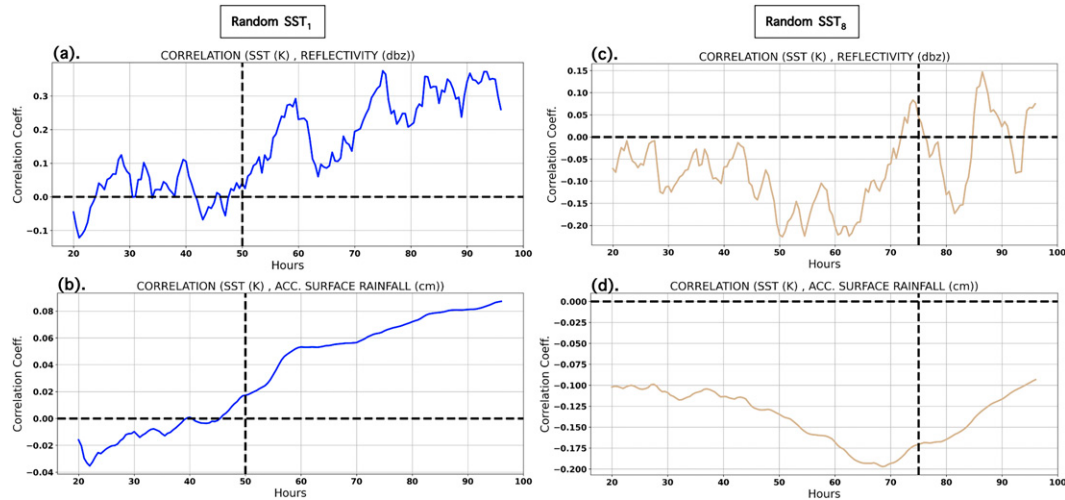


FIG. 9. Plots of spatial correlation coefficient (top) between SST and reflectivity (at 1 km altitude) and (bottom) between SST and surface accumulated rainfall for (left) Random SST₁ and (right) Random SST₈ shown in Figs. 11b and 11f, respectively. The dashed vertical line shows the timing of RI onset for both simulations.

would result in the subsequent fields having sharper gradients between anomalies, and allowing an initial vortex to be positioned over relatively larger and smaller SST anomalies. Interestingly, this increase in SST variance has no effect on the magnitude of variance in RI onset among the 36 km length-scale ensemble. This suggests that below a certain length scale (36 km in this case), an increase in the variance of the SST field realization has no effect on RI onset timing (cf. red lines in both Figs. 10 and 6a to the intrinsic variability).

In addition to results from length-scale experiment–A, length-scale experiment–B supports our hypothesis that SST length scales indeed does affect the variance in RI onset timing. This test shows that while the variance of the SST patches has a quantitative impact on the RI timing, it is the size that controls when the storm can respond. Thus, for the remainder of this paper we continue to use the realistic SST variance-size relationship.

3) THE INFLUENCE OF SCALE-INDUCED CONVECTIVE ASYMMETRIES ON RI ONSET TIMING

In this section, we address the dynamical pathways to intensification followed by the end members observed in Fig. 5, since these pathways are representative of the large variance

in RI onset among ensemble members. Asymmetries in convection around the eyewall have been shown to influence intensification of TCs (Möller and Shapiro 2005; Nolan et al. 2007; Martinez et al. 2022) depending on the spatial location and radial coverage of associated convective bursts (CB) relative to the TC eye, doing so by affecting the distribution of diabatic heating in the eyewall (Alvey et al. 2015; Rogers et al. 2016; Wadler et al. 2018; Oyama and Wada 2019). The warm SST enhances the formation of these convective systems; hence, a scale-dependent distribution of SST anomalies could induce preferential spatial distribution of convection, leading to asymmetries in convection close to the storm.

Figure 11a shows the end members (blue and light-gold solid lines) for simulations with SST length scale of 360 km that exhibit a delay of about 24 h between them. These ensemble members differ only by the spatial distribution of SST anomalies within the domain as seen in Figs. 11b, 11d, and 11f. From Figs. 11c, 11e, and 11g, there is a noticeable collocation of the 1 km simulated reflectivity signatures at 72 h in regions with relatively warmer SSTs (Figs. 11b,d,f). A comparison of Figs. 11b and 11c and Figs. 11f and 11g shows a relatively suppressed spatial distribution of convection in the SW quadrant for the latter, with convection dominantly located toward the

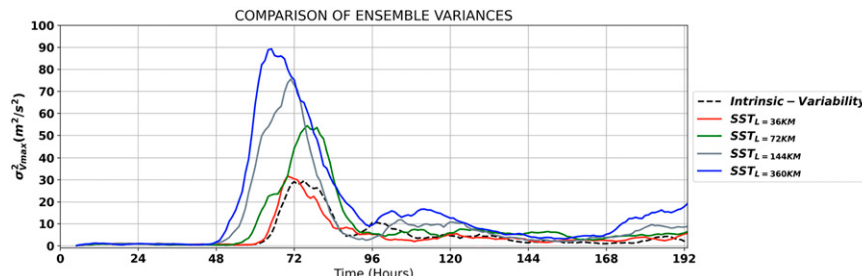


FIG. 10. As in Fig. 6a, but using constant variance in SST fields.

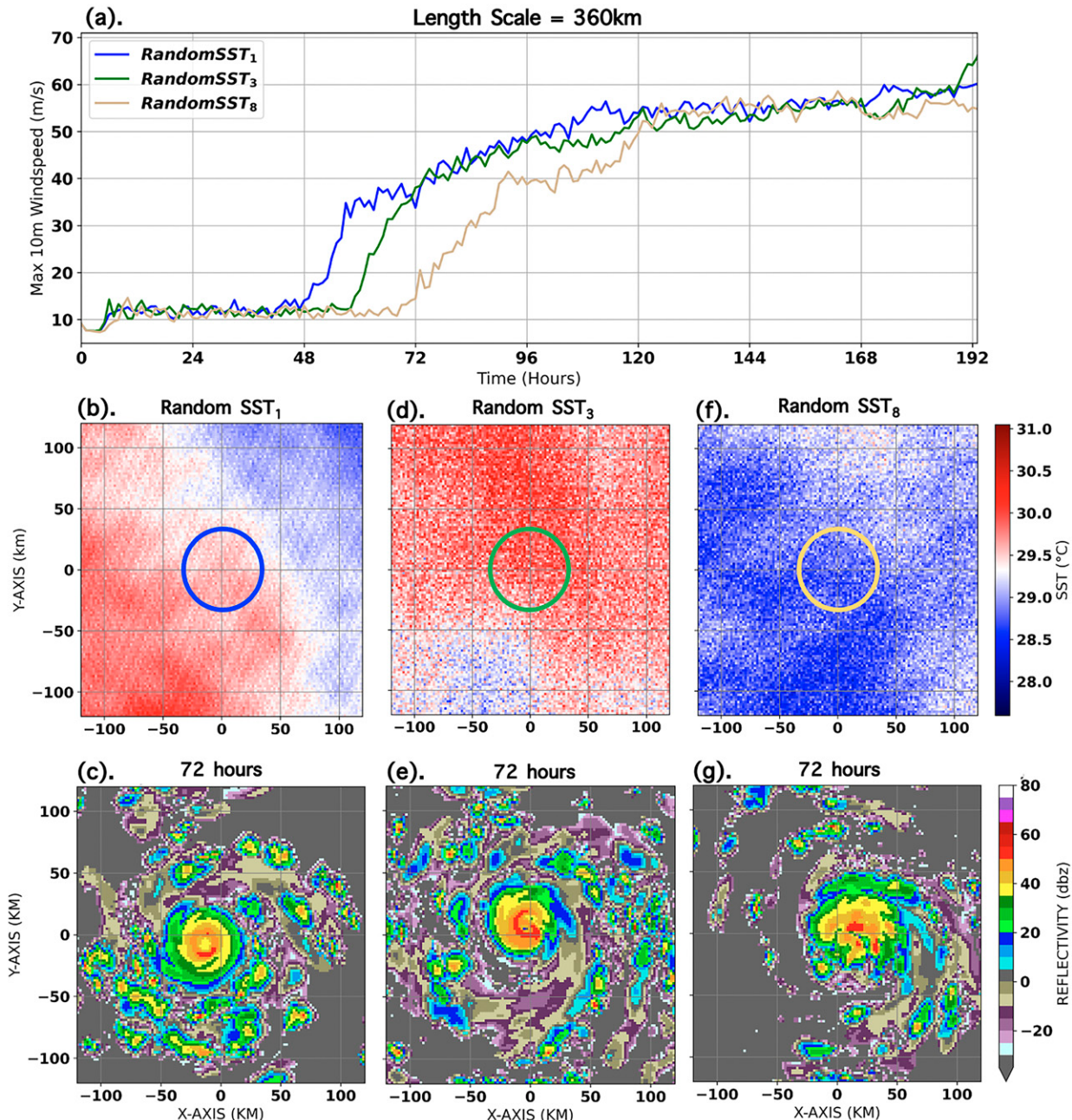


FIG. 11. (a) Intensity plots of three selected simulations (Random SST₁, Random SST₃, and Random SST₈) with a length scale of 360 km, (b),(d),(f) time-invariant SST fields for the selected three simulations shown in (a), and (c),(e),(g) simulated radar reflectivity at 72 h for the selected three simulations shown in (a).

NE quadrant where the SST progressively gets warmer. A similar pattern is visible in the former (Figs. 11b,c) where the NE quadrant lacks as many convective clusters as the SW quadrant. This suggests that the SST length scale can play an important role in the organization of convection around the storm center, with preferential development of convection over warmer SSTs leading to asymmetries in convective development. This variation in convective organization ultimately

results in variance in the onset timing of RI as seen in Fig. 11a.

Previous work (Cione and Uhlhorn 2003; Lin et al. 2009b; Kanada et al. 2017; Le Hénaff et al. 2021) has shown that warm SSTs underneath the eye/eyewall can play an important role in TC intensification. The results in Fig. 11 suggest that a comparatively warmer SST in the inner core is a necessary but not sufficient condition to guarantee an earlier RI onset.

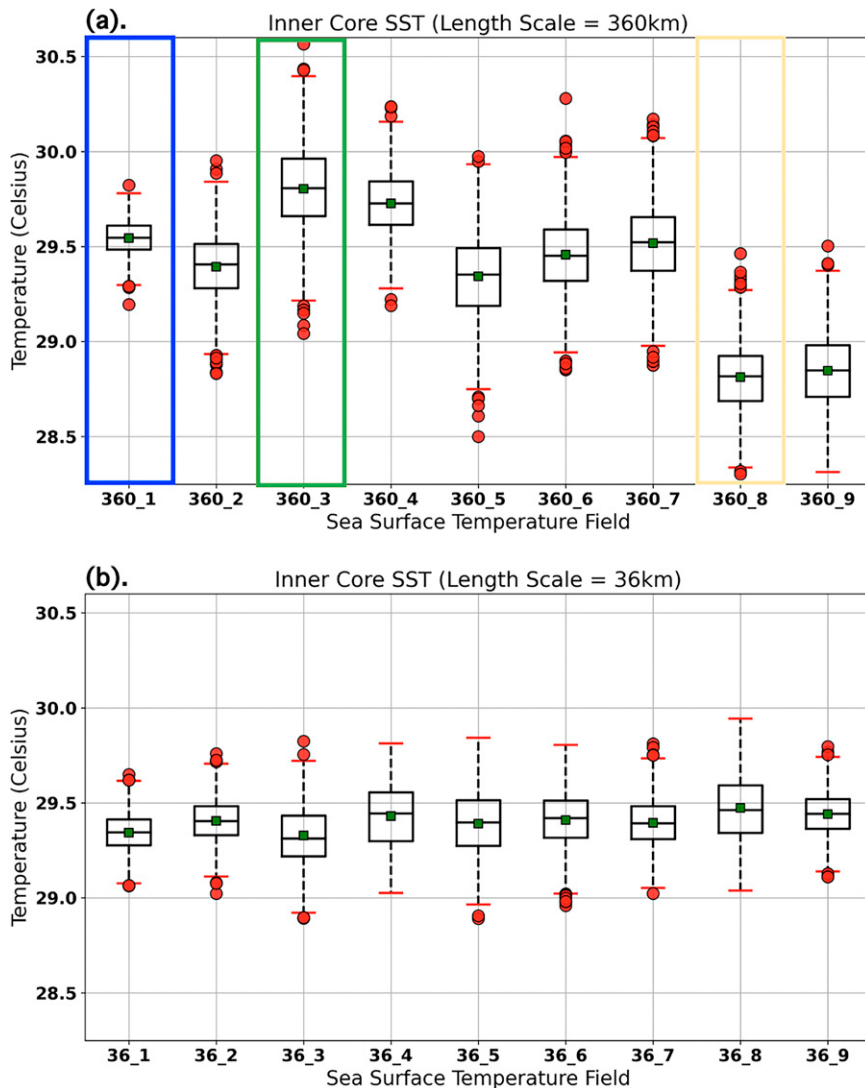


FIG. 12. Box-and-whisker plots of SST values [for (a) 360 and (b) 36 km length scales] within a 36 km radius beneath the domain center where the storm vortex was initialized. The nine box-and-whisker plots in each panel are for the nine ensemble members for each SST anomaly size.

To better quantify this, Figs. 12a and 12b present box-and-whisker plots of SST within a 36 km radius of the domain center for SST length scales of 360 and 36 km, respectively. These figures highlight a significant variance in SST for length scales of 360 km compared to length scales of 36 km. The highlighted boxplots in Fig. 12a correspond to ensemble members Random SST₁, Random SST₃, and Random SST₈ from Fig. 11. The boxplots demonstrate that a higher mean SST (indicated by the green marker in Fig. 12) within the radius of maximum wind for Random SST₃ did not necessarily lead to an earlier intensification compared to Random SST₁ with a lower mean SST. Although the strong link between SST in the eye–eyewall region and storm intensification (Cione and Uhlhorn 2003; Wadler et al. 2021) is supported by our findings (Random SST₁ and Random SST₈ in Fig. 12 and the blue and light-gold lines in Fig. 11a), our results also suggest that this

can be modulated by spatial heterogeneity in SSTs leading to asymmetry in convective development, which impacts subsequent intensification (Fig. 11b).

Comparing Figs. 5a and 12a to Figs. 5d and 12b, it is clear that the variance in SST, and not necessarily its mean value, at the core of the storm domain influences the variance in RI onset of the modeled storm. As the length scales of SST anomalies decrease from 360 to 36 km, so does the propensity for convective asymmetries induced by the larger length scales, as can be seen in Fig. 8. This suggests that larger length scales of SST heterogeneities have sufficient extent to create asymmetries in convection that can influence RI onset, unlike at smaller SST length scales where the limited spatial extent of the SST anomalies is unable to induce coherent asymmetries in convection via preferential convective development over areas of higher SST. Hence, azimuthal

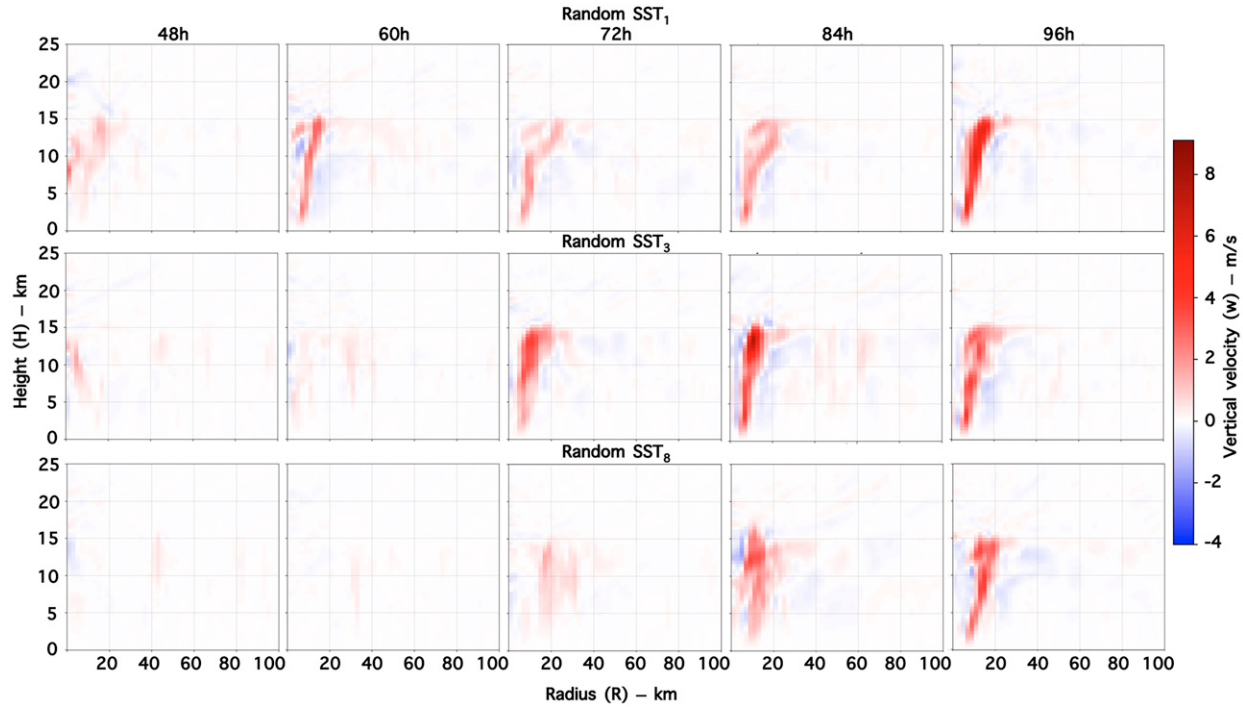


FIG. 13. Azimuthally averaged vertical velocity (m s^{-1}) from 48 to 96 h (RI phase) for (top) Random SST₁, (middle) Random SST₃, and (bottom) Random SST₈ shown in Fig. 11.

asymmetry in convection occurring with larger SST length scales, as a result of strong asymmetry in SST around the eyewall, acts to influence RI consistent with the study by Martinez et al. (2022).

To further investigate the symmetry of storm structure and possible relations to the intensification pathways shown in Fig. 11, we compare the azimuthally averaged vertical velocity for Random SST₁, Random SST₃, Random SST₈, respectively (Fig. 11) in Fig. 13. Comparing the first and third row in Fig. 13 (Random SST₁ and Random SST₈, respectively), we note that the storm initialized over a relatively warm SST anomaly (Random SST₁) forms a distinct symmetric eye structure much earlier (60 h), compared to the storm initialized over a relatively colder SST anomaly (Random SST₈) as seen in Fig. 11. This symmetric eyewall supports the rapid intensification process of the modeled storm as seen in previous literature. Comparing the first and second rows in Fig. 13 (Random SST₁ and Random SST₃, respectively), we note that even though the latter was initialized over SST conditions with high mean value (Figs. 11d and 12a), there is a noticeable delay in the timing of symmetric eyewall formation (72 h compared to 60 h for the former). Figures 11c and 11e again support this notion, with the Random SST₁ showing a clear symmetric eyewall structure compared to Random SST₃. Interestingly, we note that despite the delayed RI, strength of eyewall symmetricity is higher for Random SST₃ than in Random SST₃ as seen in Fig. 13. This suggests that the mean SST in the core most certainly influences storm intensity; however, it may not be the dominant determining factor in RI onset timing.

b. Investigating the effect of storm translation speed on the variance in RI onset timing

Previous work focused on the interaction between a translating storm and the SST suggests that slower-moving storms constrain their intensification pathway by prolonged exposure time to the self-induced cooler SST anomaly underneath the eye/eyewall itself, caused by upwelling and upper ocean mixing (Price 1981; Lin et al. 2009a). Lin et al. (2009a) concluded that a typical translation speed of $7\text{--}8 \text{ m s}^{-1}$ was sufficiently high to allow intensification up to category 5 given a shallow warm layer beneath, while slower translating storms (e.g., with translation speeds of $2\text{--}3 \text{ m s}^{-1}$) require a much deeper warm upper ocean layer to reach the same intensity.

In this section, we investigate the influence of various translation speeds on the variance in RI onset timing using a suite of uncoupled simulations with varying SST length scales. Unlike the time-invariant SST experiments in section 3a above (which were intended to isolate the contribution of the SST length scales to the variance in RI onset timing based on the storm's dynamical response to the underlying SST patterns), this section explores the role of the exposure time of modeled storms to changing length scales of SST anomalies.

Figure 14 provides a visual depiction of a sample storm translating from left to right at 2.5 and 5.0 m s^{-1} across a domain with SST anomalies corresponding to a length scale equal to 360 km (Random SST₈ in Fig. 11). From Fig. 15, we see that storms translating at any speed (2.5 or 5.0 m s^{-1}) have a generally lower variance in RI onset timing compared to stationary storm, and a higher variance compared to the

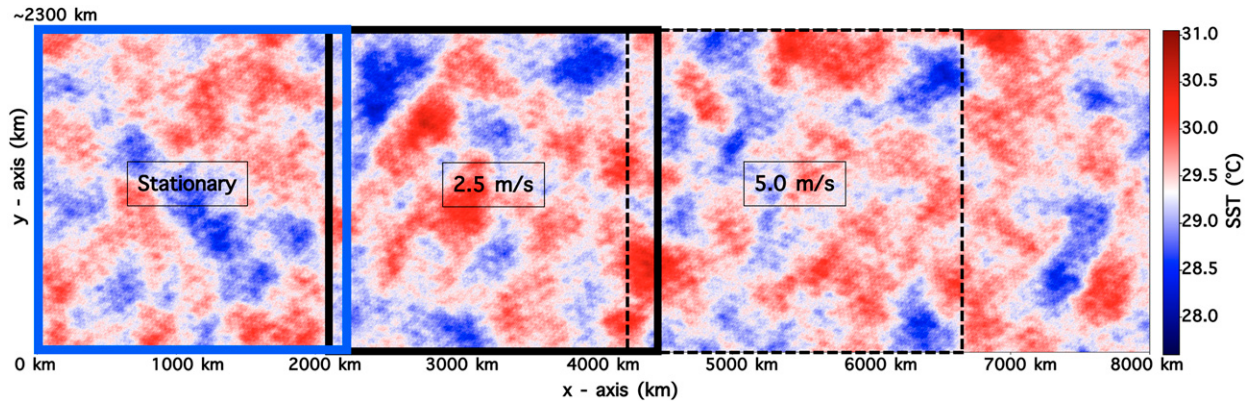


FIG. 14. Illustration of the start (solid blue box) and end location of storms translating at 2.5 and 5.0 m s^{-1} (solid and dashed black boxes, respectively) over an SST field with length scale = 360 km for 10 days (zoomed view of stationary case shown in Fig. 11f).

model intrinsic variability—both behaviors are not unexpected. The magnitude of variance in RI onset timing is seen to be roughly the same between the 2.5 m s^{-1} translation speed to 3.5 m s^{-1} translation speed experiment. However, the variance in RI onset timing seems to occur a little earlier for the slowly translating storm (2.5 m s^{-1}), suggesting that the overall effect of storm translation is to reduce the time to the onset in variance in the timing of RI among ensembles. The effect on the magnitude of this variance is less clear.

To understand the dynamics at play here, we define a time scale τ_e , characteristic of the storm exposure time to SST anomalies of a given length scale (L) and its initial RMW, given a translation speed (U_T):

$$\tau_e = \frac{\sqrt{\frac{2 \times \text{RMW} \times L}{U_T^2}}}{3600}, \quad (7)$$

where τ_e is the exposure time in hours.

Using the equation above, as expected, we see that the shortest exposure time ($\tau_e = 8.9\text{ h}$) is attributed to the storm translating over SST fields with a length scale of 360 km at the fastest translation speed ($U_T = 5.0\text{ m s}^{-1}$). On the other hand, the longest exposure time ($\tau_e = 17.9\text{ h}$) is attributed to the storm translating at $U_T = 2.5\text{ m s}^{-1}$.

Figure 15 suggests that for fast-moving storms, shorter exposure times (τ_e) to SST anomalies delays the increase in $\sigma_{V_{\max}}^2$ as the storms have less time to adjust to the SST anomaly beneath. Thus, the stationary experiments have the highest variance in RI onset timing due to the fixed SST field beneath the storm initial location: extreme warm or cold SST anomalies can cause expedited or delayed RI (Fig. 11). On the other hand, all translating storms sample a range of SSTs during their lifetime, with fast translation speeds leading to reduced exposure time and lessening the impact of any single SST anomaly on storm development. In almost all cases, however, the variability is still larger than the intrinsic variability. In the limit of very fast storm translation, we would expect the solid lines in Fig. 15 to approach the model intrinsic variability (black dashed lines) since the model storm would never be able to adjust to the SST conditions beneath it before being exposed to new SST perturbations.

Figure 16 shows the 1 km reflectivity plot after 72 h for simulated storms translating at 2.5 and 5.0 m s^{-1} across the domain. A comparison of Fig. 11c and Figs. 16a and 16b shows that convection is more symmetrically distributed about the storm translating at 2.5 and 5.0 m s^{-1} across the domain across the domain. Similarly, comparing Figs. 11e and 11g to Figs. 16c and 16e, there is a significantly improved symmetry of convection about the core of storms translating at 2.5 m s^{-1} compared

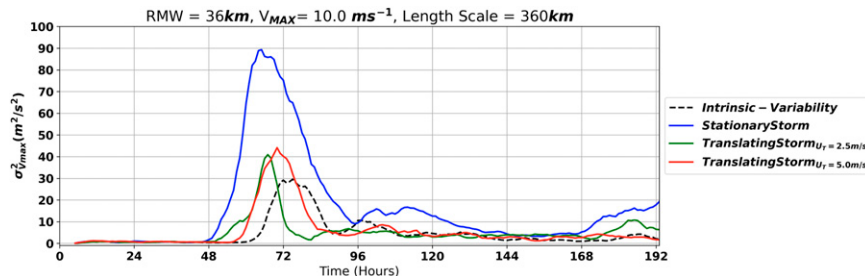


FIG. 15. Line plots of variance in maximum 10 m wind speed among ensemble simulations for a stationary storm (solid blue line), 2.5 m s^{-1} translation speed (solid green line), and 5.0 m s^{-1} translation speed (solid red line), intrinsic variability (dashed black line). Experiments are for small sized storm (RMW = 36 km) translating over SST anomalies with a length scale of 360 km .

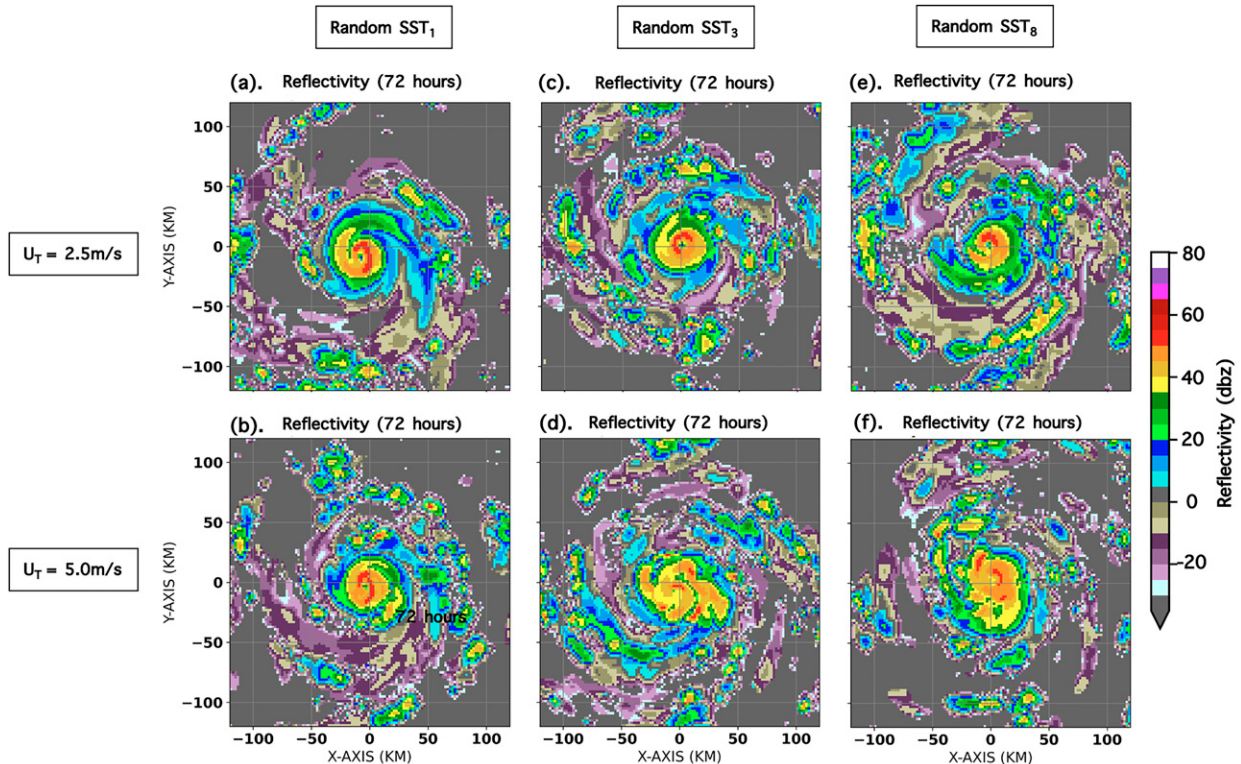


FIG. 16. As in Figs. 11c, 11e, and 11g, but with the storm translating from left to right at (top) 2.5 and (bottom) 5.0 m s^{-1} .

to the stationary case. However, as the translation speed increases to 5.0 m s^{-1} , Figs. 16d and 16f show a less symmetric eyewall structure with convection becoming less organized, suggesting that the storm structure (and by extension its intensity) does not respond linearly to increasing translation speed.

For Random SST₈, the SST field shown in Fig. 14 provides more insight into the effect of storm translation over heterogeneous SST fields on eyewall symmetry and intensity. In this case, the stationary storm simulation has its core centered around a relatively cool SST anomaly; hence, it forms the poorly organized eyewall convection seen in Fig. 11g at 72 h. However, when this storm translates slowly at 2.5 m s^{-1} , it encounters mostly warm patches of SST anomaly, enhancing convection and supporting eyewall symmetry. This, however, is not guaranteed for a faster translation speed (5.0 m s^{-1}), as it cuts across less warm anomalies. Thus, a translating storm interacting with alternating warm and cold patches of SST anomalies effectively feels the impact of the mean SST as it evolves, negating the impact of SST-induced convective asymmetries seen in the stationary case. However, the higher the translation speed, the higher the probability that the storm's core would encounter a drastically different SST conditions than where it started off. Furthermore, for the translating cases, the storm does not stay over a warm/cold patch long enough (i.e., shorter τ_c) to have its evolution significantly influenced by it. The variance among the ensemble simulations for a translating storm is thus seen to be consistently lower than that of the stationary experiments (albeit nonmonotonically

with the magnitude of storm translation speed), and is similar in magnitude to the stationary experiments with smaller length scales. This indicates that the net effect of a translating storm is analogous to that of reducing the SST length scale: i.e., reducing the variance in RI onset among the ensemble simulations by forcing an effective “mean” SST condition perceived by the evolving storm. Furthermore, we expect that for continuously increasing magnitudes of storm translation speed, the variance among the ensembles (red and green solid lines in Fig. 15) would collapse toward the model intrinsic variability (dashed black line).

Finally, a comparison of the last row in Figs. 13 and 17 illustrates the development of symmetry in vertical velocity evolving earlier for the translating storm compared to the stationary case, suggesting that delayed RI due to convective asymmetry seen in some of the stationary cases is counteracted by the translation of the storm across the domain. We note again that (from Fig. 17) the storm translating at 2.5 m s^{-1} develops a more strongly symmetric eyewall structure (first row) compared to the storm translating at 5.0 m s^{-1} (first row), supporting the spatial reflectivity plots shown above in Fig. 16. Our hypothesis that storm translation induces an effective mean SST beneath the storm (thereby reducing asymmetries which negate RI onset) is supported by the intensity plot in Fig. 18 below, as we see that the same storm translating at 2.5 m s^{-1} intensifies roughly 10–15 h earlier than when it is stationary. A closer look at Fig. 18 shows the storm with a slower translation speed of 2.5 m s^{-1} (solid black line) undergoing RI onset a

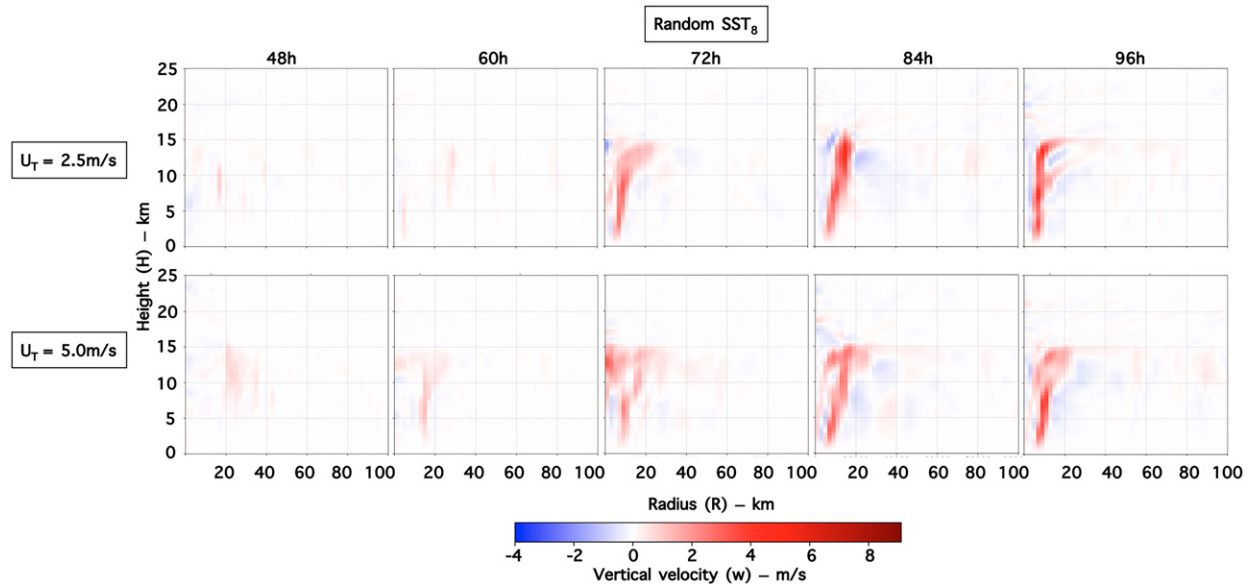


FIG. 17. As in the last row in Fig. 13, but for a storm translating from left to right at (top) 2.5 and (bottom) 5.0 m s^{-1} .

few hours earlier than the storm with a faster translation speed of 5.0 m s^{-1} . As previously explained, this is most likely due to the fact that for this specific case, the eye of the former is exposed to warmer patches between its starting and end location (Fig. 14). Another potential reason for this could be the ease of symmetric eye formation for slowly translating storms (2.5 m s^{-1}).

4. Conclusions

Geospatial statistical techniques were used to generate multiple realizations of SST fields with realistic length scales characteristic of the SST conditions during Hurricane Irma's (2017) rapid intensification. With these, we investigated the influence of SST length scales on the variance in the timing of RI onset for stationary and translating storms. We ran a total

of 90 simulations, comprising 36 suites of experiments with 9 ensemble members in each experiment, varying the length scale of SST heterogeneities and storm translation speed. This methodology allowed for a comprehensive study of the resulting variance in RI onset timing and the dynamics responsible for the different intensification pathways seen. Analyses of the variance in RI onset were based on the spatial distribution of SST and convection relative to the storm center, as well as the azimuthally averaged vertical velocity.

In agreement with previous studies, our results show that the magnitude of SST anomalies underneath the eye–eyewall region plays an important role in modulating the timing of the onset of RI. Beyond this, however, we find that SST anomalies with length scales exceeding the initial RMW induce asymmetries in convection which can act to delay RI despite the presence of favorable SST conditions within the eyewall,

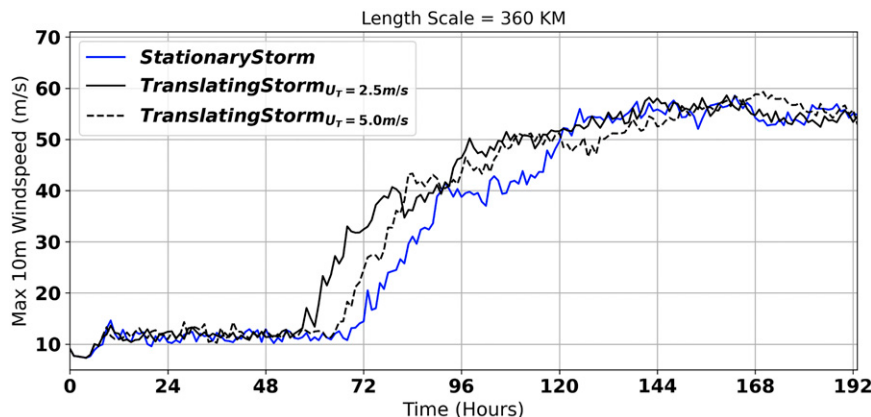


FIG. 18. Comparing the intensity evolution of a stationary and translating storm, same as the golden line plot (Random SST_8) in Fig. 11a, but with plots of the effect of various translation speeds included as solid (2.5 m s^{-1}) and dashed (5.0 m s^{-1}) black lines.

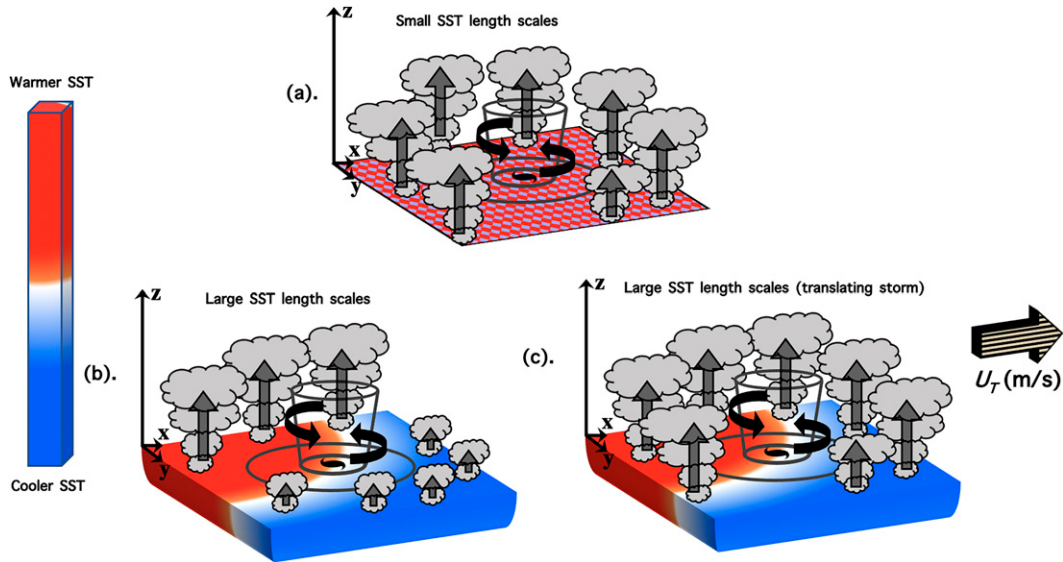


FIG. 19. Schematics showing updraft and spatial distribution of convection and convective bursts induced by the magnitude of SST length scales for (a) small length scales, (b) larger length scales, and (c) larger length scales with a storm translating at U_T , relative to the storm center. The red and blue region represent relatively warmer and cooler SSTs.

and despite the same domain-averaged mean SST. Furthermore, the reduced exposure time of a translating storm to SST anomalies of a prescribed length, compared to a stationary storm, is seen to modulate the effect of the SST anomalies on storm development. At higher translation speeds, the storm feels the effect of a particular SST anomaly for a relatively short time, rather experiencing the effective mean SST conditions, akin to the small SST length-scale experiments in section 3b. Thus, higher translation speeds reduce azimuthal asymmetries in convection by preventing the preferential development of convection over stationary warm SST anomalies, which removes a potential barrier to intensification.

An interplay between the above processes is seen to modulate the variance in RI onset timing among the ensemble members. Key findings from this study are summarized below:

- 1) For stationary storms in the presence of SST anomalies (Figs. 19a,b), we find that the magnitude of the SST anomaly underneath the eye–eyewall region alone does not control the RI regime seen in modeled storms. However, in addition to this, the length scale of these anomalies modulates the preferential distribution of convective development beyond the eyewall, creating asymmetries that significantly influence the timing of RI onset among the ensemble members. Smaller length scales lack the spatial extent to induce these convective asymmetries (Fig. 19a); hence, ensembles in a small length-scale field “feel” an effective mean SST.
- 2) The variance in RI onset timing among ensembles of translating experiments is seen to be lower than that of the stationary storm experiments, irrespective of the translation speed. Furthermore, we find that the storm exposure time to SST anomalies (τ_e), plays a crucial role in the dynamics seen for translating storms.
- 3) For translating storms in the presence of SST anomalies (Fig. 19c), the convective asymmetries induced in the stationary case (Fig. 19b) is minimal. This suggests that the net effect of translation over warm and cold patches is to reduce the variance in RI onset timing among ensembles by forcing the storm to experience a net “mean” SST analogous to the stationary case over small length scales of SST anomalies (as illustrated in Figs. 19a,c).

Figure 19 shows a conceptual framework of the key findings in this study, summarizing points 1–3 above. In agreement with previous work (Möller and Shapiro 2005), our results demonstrate that preexisting anomalies in underlying ocean conditions (in our case, SST perturbations) can have significant impacts for the intensification of tropical cyclones through imposed convective asymmetries. The consequence of our findings for the predictability of TC RI is that storms encountering multiscale SST anomalies would have a variance in RI onset timing that would be higher for larger SST length scales (specifically those exceeding $2 \times \text{RMW}$). The speed of TC translation reduces this variance and thus increases predictability but does not eliminate it. Thus, in favorable atmospheric conditions, RI predictability is highest in near-homogeneous SST conditions (in an uncoupled model) or for SST anomalies (or eddies) that are much less than mesoscale (~ 100 km or greater). One possible direct application of the findings from this study is the inclusion of horizontal gradient/length scales of SST anomalies in statistical-dynamical models which include SST as a predictor like the Statistical Hurricane Intensity Prediction Scheme (SHIPS) (DeMaria and Kaplan 1994, 1999) or SHIPS-RII. Conclusively, this study shows that convective organization relative to the storm center can significantly influence intensification even in the presence of warm inner-core SST conditions.

While this study details the importance of SST length scales in modulating RI onset timing, it is important to acknowledge that the use of an idealized model setup favorable for RI onset does not always represent realistic conditions in the TC environment. Limitations in the numerical setup used here include the exclusion of vertical wind shear, which if present can limit TC intensification through dry-air intrusion into the core and vortex tilting (Zhang and Tao 2013; Finocchio et al. 2016; Tao and Zhang 2019; Alland et al. 2021). Furthermore, all simulations presented here are uncoupled (not including an ocean model or mixed layer model). Nevertheless, our results provide evidence for the importance of SST length scales on air-sea interaction and subsequent TC intensification, and this factor should be considered in ongoing efforts to understand the dynamics of RI and better predict it.

Acknowledgments. The authors would like to acknowledge George Bryan of the National Center for Atmospheric Research (NCAR) for making the model code (CM1) used in this study publicly available. We also acknowledge Drs. Steven Jayne and Elizabeth Sanabia for providing the ALAMO float dataset shown in this study. We acknowledge the ONR N00014-19-S-B001 Grant for financial support under the Tropical Cyclone Rapid Intensification (TCRI) campaign. Computing and storage resources used for all simulations presented in this study were made available through the University of Notre Dame Center for Research

Computing (CRC). We acknowledge useful conversations with Dr. David Nolan.

Data availability statement. Model simulation outputs from CM1 are available upon request. Argo and ALAMO float data are publicly available from <https://argo.ucsd.edu/data/data-from-gdacs/> and <https://www.ncei.noaa.gov/access/metadata/landing-page/bin/iso?id=gov.noaa.nodc:0210577>, respectively. The 1 km NASA MODIS SST product can be downloaded online from the Amazon Web Services (AWS) repository at <https://registry.opendata.aws/mur/>.

APPENDIX A

Ocean Observation of SST during Hurricane Irma's (2017) Passage

Temperature measurements from ALAMO floats beneath Hurricane Irma (2017), which were extensively analyzed in [Sanabia and Jayne \(2020\)](#), are shown in Figs. A1a–d. Floats 9126 and 9134 are closest to the storm and located to the left and right, respectively, while 9129 and 9143 are located farthest from the storm (see Fig. 2b). Regardless of our use of uncoupled simulations, Figs. A1a–d provide observational evidence of spatial and temporal variation in SST relative to the storm center, in addition to Fig. 2c. There is a clear deepening of the mixed layer depth (seen in floats 9134 between the fifth and sixth days) due to storm-induced upwelling as a consequence of Irma's passage.

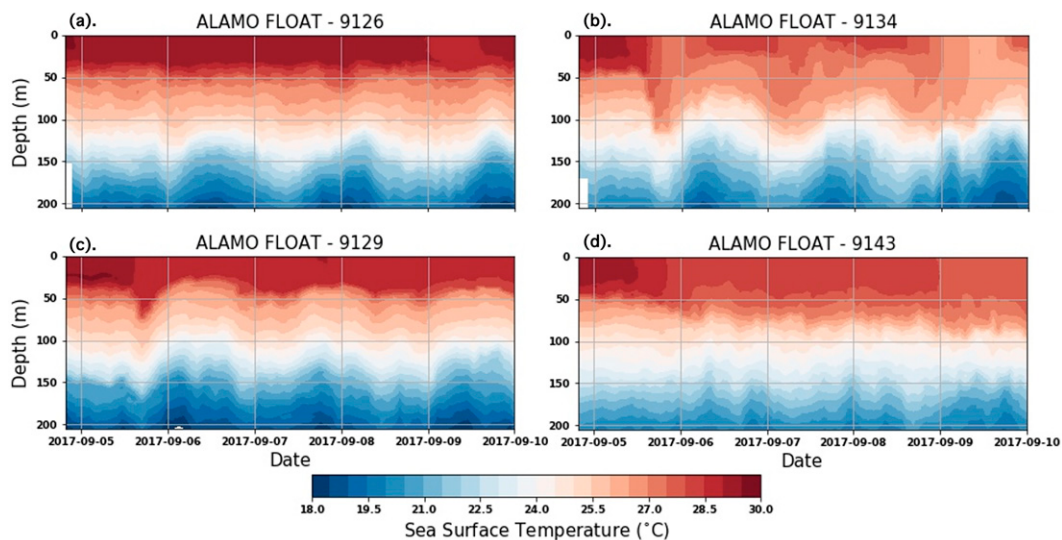


FIG. A1. Temporal variation of upper-ocean temperature, measured from four selected ALAMO floats distributed across the path of Hurricane Irma (2017) as shown in Fig. 2b.

APPENDIX B

Variogram Estimation and Anisotropy

From the SST field provided in Fig. 2a, experimental variograms shown in Figs. B1 and B2 were computed using the Matheron estimator [Eq. (5)] implemented in the SciKit Gstat Python (Mälicke 2022). For the omnidirectional variogram (ignoring anisotropic effects) shown in Fig. A1, 4000 random pairs of spatial locations, 45 bins of lag classes, and a maximum lag of 280 grid points (i.e., 560 km) were used.

Directional variograms (shown in Fig. B2) were also computed for the N–S and E–W direction using an azimuth of 90° and 0° , respectively. The directional variograms were computed using similar parameters as the omnidirectional variogram, but for a 15° tolerance about the respective azimuth. From Fig. B2a, we see that the experimental variograms for both N–S and E–W directions track along each other up until a lag distance of about 230 grid points, suggesting that there is no preferred direction of spatial coherence up until that length scale. After this lag distance, the N–S directional variogram is seen to plateau, while the E–W directional variogram continues to increase. This indicates that up to a length scale of 230 grid points (560 km), there is no preferred direction of spatial continuity in the SST field, partially justifying our assumption of isotropy in the realizations of SST fields generated.

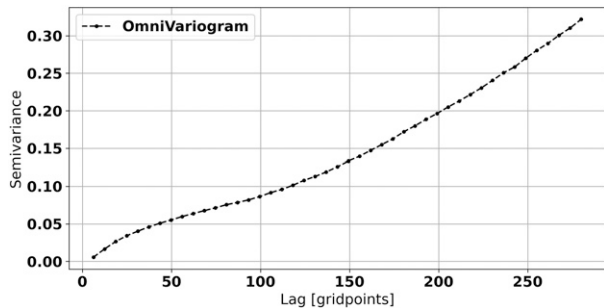


FIG. B1. Experimental omnidirectional variogram (N–S and E–W directions) of the SST field traversed by Hurricane Irma (2017).

Figures B2b and B2c show the same directional experimental variograms in Fig. B2a, fitted with zero-nugget spherical variograms (shown by the green lines). From Fig. B2c, we see that the spherical theoretical variogram reasonably captures the behavior of the experimental variogram, hence justifying our choice to generate random SST fields using the spherical variogram. We utilized the gstools Python framework (Müller et al. 2022) for generating spatial random fields (SRF) using a well-known spectral method known as the randomization approach, which we opted for due to its improved computational efficiency (Heße et al. 2014).

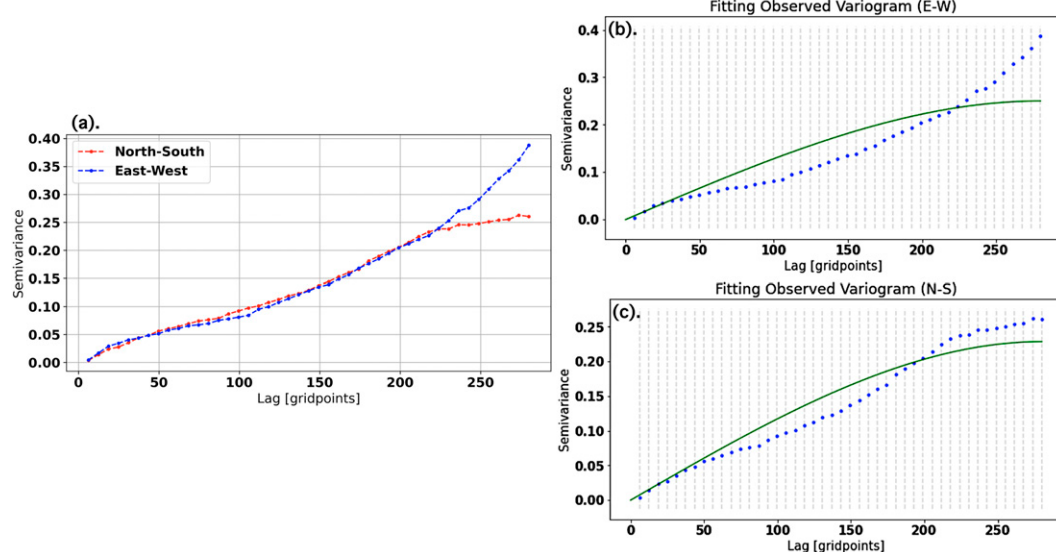


FIG. B2. (a) Experimental directional variogram (N–S and E–W directions) of the SST field traversed by Hurricane Irma (2017), (b) experimental variogram for E–W direction fitted with spherical theoretical variogram, and (c) experimental variogram for N–S direction fitted with spherical theoretical variogram.

REFERENCES

- Alland, J. J., B. H. Tang, K. L. Corbosiero, and G. H. Bryan, 2021: Combined effects of midlevel dry air and vertical wind shear on tropical cyclone development. Part II: Radial ventilation. *J. Atmos. Sci.*, **78**, 783–796, <https://doi.org/10.1175/JAS-D-20-0055.1>.
- Alvey, G. R., III, J. Zawislak, and E. Zipser, 2015: Precipitation properties observed during tropical cyclone intensity change. *Mon. Wea. Rev.*, **143**, 4476–4492, <https://doi.org/10.1175/MWR-D-15-0065.1>.
- Anandh, T. S., B. K. Das, J. Kuttipurath, and A. Chakraborty, 2020: A coupled model analyses on the interaction between oceanic eddies and tropical cyclones over the Bay of Bengal. *Ocean Dyn.*, **70**, 327–337, <https://doi.org/10.1007/s10236-019-01330-x>.
- Bryan, G. H., and J. M. Fritsch, 2002: A benchmark simulation for moist nonhydrostatic numerical models. *Mon. Wea. Rev.*, **130**, 2917–2928, [https://doi.org/10.1175/1520-0493\(2002\)130<2917:ABSFMN>2.0.CO;2](https://doi.org/10.1175/1520-0493(2002)130<2917:ABSFMN>2.0.CO;2).
- , and R. Rotunno, 2009: The maximum intensity of tropical cyclones in axisymmetric numerical model simulations. *Mon. Wea. Rev.*, **137**, 1770–1789, <https://doi.org/10.1175/2008MWR2709.1>.
- Carrasco, C. A., C. W. Landsea, and Y.-L. Lin, 2014: The influence of tropical cyclone size on its intensification. *Wea. Forecasting*, **29**, 582–590, <https://doi.org/10.1175/WAF-D-13-00092.1>.
- Chelton, D. B., M. G. Schlax, and R. M. Samelson, 2011: Global observations of nonlinear mesoscale eddies. *Prog. Oceanogr.*, **91**, 167–216, <https://doi.org/10.1016/j.pocean.2011.01.002>.
- Chen, S., R. L. Elsberry, and P. A. Harr, 2017: Modeling interaction of a tropical cyclone with its cold wake. *J. Atmos. Sci.*, **74**, 3981–4001, <https://doi.org/10.1175/JAS-D-16-0246.1>.
- Cheng, Y.-H., C.-R. Ho, Q. Zheng, and N.-J. Kuo, 2014: Statistical characteristics of mesoscale eddies in the North Pacific derived from satellite altimetry. *Remote Sens.*, **6**, 5164–5183, <https://doi.org/10.3390/rs6065164>.
- Chin, T. M., J. Vazquez-Cuervo, and E. M. Armstrong, 2017: A multi-scale high-resolution analysis of global sea surface temperature. *Remote Sens. Environ.*, **200**, 154–169, <https://doi.org/10.1016/j.rse.2017.07.029>.
- Cione, J. J., and E. W. Uhlhorn, 2003: Sea surface temperature variability in hurricanes: Implications with respect to intensity change. *Mon. Wea. Rev.*, **131**, 1783–1796, <https://doi.org/10.1175/2562.1>.
- Clark, I., 1979: *Practical Geostatistics*. Applied Science Publishers, 129 pp.
- Cressie, N. A., 1993: *Statistics for Spatial Data*. John Wiley and Sons, 928 pp.
- DeMaria, M., and J. Kaplan, 1994: A Statistical Hurricane Intensity Prediction Scheme (SHIPS) for the Atlantic basin. *Wea. Forecasting*, **9**, 209–220, [https://doi.org/10.1175/1520-0434\(1994\)009<0209:ASHIPS>2.0.CO;2](https://doi.org/10.1175/1520-0434(1994)009<0209:ASHIPS>2.0.CO;2).
- , and —, 1999: An updated Statistical Hurricane Intensity Prediction Scheme (SHIPS) for the Atlantic and eastern North Pacific basins. *Wea. Forecasting*, **14**, 326–337, [https://doi.org/10.1175/1520-0434\(1999\)014<0326:AUSHIP>2.0.CO;2](https://doi.org/10.1175/1520-0434(1999)014<0326:AUSHIP>2.0.CO;2).
- Doney, S. C., D. M. Glover, S. J. McCue, and M. Fuentes, 2003: Mesoscale variability of Sea-Viewing Wide Field-Of-View Sensor (SeaWiFS) satellite ocean color: Global patterns and spatial scales. *J. Geophys. Res.*, **108**, 3024, <https://doi.org/10.1029/2001JC000843>.
- Emanuel, K. A., 1986: An air-sea interaction theory for tropical cyclones. Part I: Steady-state maintenance. *J. Atmos. Sci.*, **43**, 585–605, [https://doi.org/10.1175/1520-0469\(1986\)043<0585:AASITF>2.0.CO;2](https://doi.org/10.1175/1520-0469(1986)043<0585:AASITF>2.0.CO;2).
- , 1988: The maximum intensity of hurricanes. *J. Atmos. Sci.*, **45**, 1143–1155, [https://doi.org/10.1175/1520-0469\(1988\)045<1143:TMIOH>2.0.CO;2](https://doi.org/10.1175/1520-0469(1988)045<1143:TMIOH>2.0.CO;2).
- , 1995: Sensitivity of tropical cyclones to surface exchange coefficients and a revised steady-state model incorporating eye dynamics. *J. Atmos. Sci.*, **52**, 3969–3976, [https://doi.org/10.1175/1520-0469\(1995\)052<3969:SOTCTS>2.0.CO;2](https://doi.org/10.1175/1520-0469(1995)052<3969:SOTCTS>2.0.CO;2).
- , C. DesAutels, C. Holloway, and R. Korty, 2004: Environmental control of tropical cyclone intensity. *J. Atmos. Sci.*, **61**, 843–858, [https://doi.org/10.1175/1520-0469\(2004\)061<0843:ECOTCI>2.0.CO;2](https://doi.org/10.1175/1520-0469(2004)061<0843:ECOTCI>2.0.CO;2).
- Finocchio, P. M., S. J. Majumdar, D. S. Nolan, and M. Iskandarani, 2016: Idealized tropical cyclone responses to the height and depth of environmental vertical wind shear. *Mon. Wea. Rev.*, **144**, 2155–2175, <https://doi.org/10.1175/MWR-D-15-0320.1>.
- Haakman, K., J.-M. Sayol, C. G. van der Boog, and C. A. Katsman, 2019: Statistical characterization of the observed cold wake induced by North Atlantic hurricanes. *Remote Sens.*, **11**, 2368, <https://doi.org/10.3390/rs11202368>.
- Hemingway, B. L., A. E. Frazier, B. R. Elbing, and J. D. Jacob, 2020: High-resolution estimation and spatial interpolation of temperature structure in the atmospheric boundary layer using a small unmanned aircraft system. *Bound.-Layer Meteor.*, **175**, 397–416, <https://doi.org/10.1007/s10546-020-00512-1>.
- Heße, F., V. Prykhodko, S. Schlüter, and S. Attinger, 2014: Generating random fields with a truncated power-law variogram: A comparison of several numerical methods. *Environ. Model. Software*, **55**, 32–48, <https://doi.org/10.1016/j.envsoft.2014.01.013>.
- Holland, G. J., 1997: The maximum potential intensity of tropical cyclones. *J. Atmos. Sci.*, **54**, 2519–2541, [https://doi.org/10.1175/1520-0469\(1997\)054<2519:TMPIOT>2.0.CO;2](https://doi.org/10.1175/1520-0469(1997)054<2519:TMPIOT>2.0.CO;2).
- , and R. T. Merrill, 1984: On the dynamics of tropical cyclone structural changes. *Quart. J. Roy. Meteor. Soc.*, **110**, 723–745, <https://doi.org/10.1002/qj.49711046510>.
- Jaimes de la Cruz, B., L. K. Shay, J. B. Wadler, and J. E. Rudzin, 2021: On the hyperbolicity of the bulk air-sea heat flux functions: Insights into the efficiency of air-sea moisture disequilibrium for tropical cyclone intensification. *Mon. Wea. Rev.*, **149**, 1517–1534, <https://doi.org/10.1175/MWR-D-20-0324.1>.
- Journel, A. G., and C. J. Huijbregts, 1978: *Mining Geostatistics*. Academic Press, 600 pp.
- Kanada, S., S. Tsujino, H. Aiki, M. K. Yoshioka, Y. Miyazawa, K. Tsuboki, and I. Takayabu, 2017: Impacts of SST patterns on rapid intensification of Typhoon Megi (2010). *J. Geophys. Res. Atmos.*, **122**, 13 245–13 262, <https://doi.org/10.1002/2017JD027252>.
- Karnauskas, K. B., L. Zhang, and K. A. Emanuel, 2021: The feedback of cold wakes on tropical cyclones. *Geophys. Res. Lett.*, **48**, e2020GL091676, <https://doi.org/10.1029/2020GL091676>.
- Kossin, J. P., 2018: A global slowdown of tropical-cyclone translation speed. *Nature*, **558**, 104–107, <https://doi.org/10.1038/s41586-018-0158-3>.
- Le Hénaff, M., and Coauthors, 2021: The role of the Gulf of Mexico Ocean conditions in the intensification of Hurricane Michael (2018). *J. Geophys. Res. Oceans*, **126**, e2020JC016969, <https://doi.org/10.1029/2020JC016969>.
- Lin, I.-I., C.-C. Wu, K. A. Emanuel, I.-H. Lee, C.-R. Wu, and I.-F. Pun, 2005: The interaction of Supertyphoon Maemi (2003)

- with a warm ocean eddy. *Mon. Wea. Rev.*, **133**, 2635–2649, <https://doi.org/10.1175/MWR3005.1>.
- , I.-F. Pun, and C.-C. Wu, 2009a: Upper-ocean thermal structure and the western North Pacific category 5 typhoons. Part II: Dependence on translation speed. *Mon. Wea. Rev.*, **137**, 3744–3757, <https://doi.org/10.1175/2009MWR2713.1>.
- , C.-H. Chen, I.-F. Pun, W. T. Liu, and C.-C. Wu, 2009b: Warm ocean anomaly, air sea fluxes, and the rapid intensification of Tropical Cyclone Nargis (2008). *Geophys. Res. Lett.*, **36**, L03817, <https://doi.org/10.1029/2008GL035815>.
- , M.-D. Chou, and C.-C. Wu, 2011: The impact of a warm ocean eddy on Typhoon Morakot (2009): A preliminary study from satellite observations and numerical modelling. *Terr. Atmos. Ocean. Sci.*, **22**, 661–671, [https://doi.org/10.3319/TAO.2011.08.19.01\(TM\)](https://doi.org/10.3319/TAO.2011.08.19.01(TM)).
- Liu, Y., C. Dong, Y. Guan, D. Chen, J. McWilliams, and F. Nencioli, 2012: Eddy analysis in the subtropical zonal band of the North Pacific Ocean. *Deep-Sea Res. I*, **68**, 54–67, <https://doi.org/10.1016/j.dsr.2012.06.001>.
- , H. Lü, H. Zhang, Y. Cui, and X. Xing, 2021: Effects of ocean eddies on the Tropical Storm Roanu intensity in the Bay of Bengal. *PLOS ONE*, **16**, e0247521, <https://doi.org/10.1371/journal.pone.0247521>.
- Ma, Z., J. Fei, L. Liu, X. Huang, and Y. Li, 2017: An investigation of the influences of mesoscale ocean eddies on tropical cyclone intensities. *Mon. Wea. Rev.*, **145**, 1181–1201, <https://doi.org/10.1175/MWR-D-16-0253.1>.
- Mälicke, M., 2022: SciKit-GStat 1.0: A SciPy-flavored geostatistical variogram estimation toolbox written in Python. *Geosci. Model Dev.*, **15**, 2505–2532, <https://doi.org/10.5194/gmd-15-2505-2022>.
- Martinez, J., C. A. Davis, and M. M. Bell, 2022: Eyewall asymmetries and their contributions to the intensification of an idealized tropical cyclone translating in uniform flow. *J. Atmos. Sci.*, **79**, 2471–2491, <https://doi.org/10.1175/JAS-D-21-0302.1>.
- Matheron, G., 1965: *The Theory of Regionalized Variables and Their Estimation: An Application of the Theory of Random Functions to the Natural Sciences*. Vol. 4597. Masson and CIE, 305 pp.
- Mei, W., C. Pasquero, and F. Primeau, 2012: The effect of translation speed upon the intensity of tropical cyclones over the tropical ocean. *Geophys. Res. Lett.*, **39**, L07801, <https://doi.org/10.1029/2011GL050765>.
- Möller, J. D., and L. J. Shapiro, 2005: Influences of asymmetric heating on hurricane evolution in the MM5. *J. Atmos. Sci.*, **62**, 3974–3992, <https://doi.org/10.1175/JAS3577.1>.
- Morrison, H., J. A. Curry, and V. I. Khvorostyanov, 2005: A new double-moment microphysics parameterization for application in cloud and climate models. Part I: Description. *J. Atmos. Sci.*, **62**, 1665–1677, <https://doi.org/10.1175/JAS3446.1>.
- , G. Thompson, and V. Tatarksi, 2009: Impact of cloud microphysics on the development of trailing stratiform precipitation in a simulated squall line: Comparison of one- and two-moment schemes. *Mon. Wea. Rev.*, **137**, 991–1007, <https://doi.org/10.1175/2008MWR2556.1>.
- Mrvaljevic, R. K., and Coauthors, 2013: Observations of the cold wake of Typhoon Fanapi (2010). *Geophys. Res. Lett.*, **40**, 316–321, <https://doi.org/10.1029/2012GL054282>.
- Müller, S., L. Schüler, A. Zech, and F. Heße, 2022: GSTools v1.3: A toolbox for geostatistical modelling in Python. *Geosci. Model Dev.*, **15**, 3161–3182, <https://doi.org/10.5194/gmd-15-3161-2022>.
- Nolan, D. S., Y. Moon, and D. P. Stern, 2007: Tropical cyclone intensification from asymmetric convection: Energetics and efficiency. *J. Atmos. Sci.*, **64**, 3377–3405, <https://doi.org/10.1175/JAS3988.1>.
- Oyama, R., and A. Wada, 2019: The relationship between convective bursts and warm-core intensification in a nonhydrostatic simulation of Typhoon Lionrock (2016). *Mon. Wea. Rev.*, **147**, 1557–1579, <https://doi.org/10.1175/MWR-D-18-0457.1>.
- Price, J. F., 1981: Upper ocean response to a hurricane. *J. Phys. Oceanogr.*, **11**, 153–175, [https://doi.org/10.1175/1520-0485\(1981\)011<0153:UORTAH>2.0.CO;2](https://doi.org/10.1175/1520-0485(1981)011<0153:UORTAH>2.0.CO;2).
- , J. Morzel, and P. P. Niiler, 2008: Warming of SST in the cool wake of a moving hurricane. *J. Geophys. Res.*, **113**, C07010, <https://doi.org/10.1029/2007JC004393>.
- Rogers, R. F., J. A. Zhang, J. Zawislak, H. Jiang, G. R. Alvey III, E. J. Zipser, and S. N. Stevenson, 2016: Observations of the structure and evolution of Hurricane Edouard (2014) during intensity change. Part II: Kinematic structure and the distribution of deep convection. *Mon. Wea. Rev.*, **144**, 3355–3376, <https://doi.org/10.1175/MWR-D-16-0017.1>.
- Rudzin, J. E., L. K. Shay, and B. Jaimes de la Cruz, 2019: The impact of the Amazon–Orinoco River plume on enthalpy flux and air-sea interaction within Caribbean Sea tropical cyclones. *Mon. Wea. Rev.*, **147**, 931–950, <https://doi.org/10.1175/MWR-D-18-0295.1>.
- , S. Chen, E. R. Sanabia, and S. R. Jayne, 2020: The air-sea response during Hurricane Irma’s (2017) rapid intensification over the Amazon-Orinoco River plume as measured by atmospheric and oceanic observations. *J. Geophys. Res. Atmos.*, **125**, e2019JD032368, <https://doi.org/10.1029/2019JD032368>.
- Sanabia, E. R., and S. R. Jayne, 2020: Ocean observations under two major hurricanes: Evolution of the response across the storm wakes. *AGU Adv.*, **1**, e2019AV000161, <https://doi.org/10.1029/2019AV000161>.
- Schade, L. R., and K. A. Emanuel, 1999: The ocean’s effect on the intensity of tropical cyclones: Results from a simple coupled atmosphere–ocean model. *J. Atmos. Sci.*, **56**, 642–651, [https://doi.org/10.1175/1520-0469\(1999\)056<0642:TOSEOT>2.0.CO;2](https://doi.org/10.1175/1520-0469(1999)056<0642:TOSEOT>2.0.CO;2).
- Shay, L. K., G. J. Goni, and P. G. Black, 2000: Effects of a warm oceanic feature on Hurricane Opal. *Mon. Wea. Rev.*, **128**, 1366–1383, [https://doi.org/10.1175/1520-0493\(2000\)128<1366:EOAWOF>2.0.CO;2](https://doi.org/10.1175/1520-0493(2000)128<1366:EOAWOF>2.0.CO;2).
- Sun, J., and Coauthors, 2020: Impact of warm mesoscale eddy on tropical cyclone intensity. *Acta Oceanol. Sin.*, **39** (8), 1–13, <https://doi.org/10.1007/s13131-020-1617-x>.
- Tao, D., and F. Zhang, 2019: Evolution of dynamic and thermodynamic structures before and during rapid intensification of tropical cyclones: Sensitivity to vertical wind shear. *Mon. Wea. Rev.*, **147**, 1171–1191, <https://doi.org/10.1175/MWR-D-18-0173.1>.
- Wadler, J. B., R. F. Rogers, and P. D. Reasor, 2018: The relationship between spatial variations in the structure of convective bursts and tropical cyclone intensification as determined by airborne Doppler radar. *Mon. Wea. Rev.*, **146**, 761–780, <https://doi.org/10.1175/MWR-D-17-0213.1>.
- , J. A. Zhang, R. F. Rogers, B. Jaimes, and L. K. Shay, 2021: The rapid intensification of Hurricane Michael (2018): Storm structure and the relationship to environmental and air-sea interactions. *Mon. Wea. Rev.*, **149**, 245–267, <https://doi.org/10.1175/MWR-D-20-0145.1>.
- Webster, R., and M. A. Oliver, 2007: *Geostatistics for Environmental Scientists*. John Wiley and Sons, 336 pp.

- Wu, C.-C., C.-Y. Lee, and I.-I. Lin, 2007: The effect of the ocean eddy on tropical cyclone intensity. *J. Atmos. Sci.*, **64**, 3562–3578, <https://doi.org/10.1175/JAS4051.1>.
- Wu, L., B. Wang, and S. A. Braun, 2005: Impacts of air-sea interaction on tropical cyclone track and intensity. *Mon. Wea. Rev.*, **133**, 3299–3314, <https://doi.org/10.1175/MWR3030.1>.
- Xu, F., and A. Ignatov, 2010: Evaluation of in situ sea surface temperatures for use in the calibration and validation of satellite retrievals. *J. Geophys. Res.*, **115**, C09022, <https://doi.org/10.1029/2010JC006129>.
- , and —, 2014: In situ SST Quality Monitor (*iQuam*). *J. Atmos. Oceanic Technol.*, **31**, 164–180, <https://doi.org/10.1175/JTECH-D-13-00121.1>.
- , and —, 2016: Error characterization in *iQuam* SSTs using triple collocations with satellite measurements. *Geophys. Res. Lett.*, **43**, 10 826–10 834, <https://doi.org/10.1002/2016GL070287>.
- Yang, G., F. Wang, Y. Li, and P. Lin, 2013: Mesoscale eddies in the northwestern subtropical Pacific Ocean: Statistical characteristics and three-dimensional structures. *J. Geophys. Res. Oceans*, **118**, 1906–1925, <https://doi.org/10.1002/jgrc.20164>.
- , W. Yu, Y. Yuan, X. Zhao, F. Wang, G. Chen, L. Liu, and Y. Duan, 2015: Characteristics, vertical structures, and heat/salt transports of mesoscale eddies in the southeastern tropical Indian Ocean. *J. Geophys. Res. Oceans*, **120**, 6733–6750, <https://doi.org/10.1002/2015JC011130>.
- Zhang, F., and D. Tao, 2013: Effects of vertical wind shear on the predictability of tropical cyclones. *J. Atmos. Sci.*, **70**, 975–983, <https://doi.org/10.1175/JAS-D-12-0133.1>.
- Zhang, J., Y. Lin, D. R. Chavas, and W. Mei, 2019: Tropical cyclone cold wake size and its applications to power dissipation and ocean heat uptake estimates. *Geophys. Res. Lett.*, **46**, 10 177–10 185, <https://doi.org/10.1029/2019GL083783>.